

PAPER

Predictive multi-channel flux-driven modelling to optimise ICRH tungsten control and fusion performance in JET

To cite this article: F.J. Casson *et al* 2020 *Nucl. Fusion* **60** 066029

View the [article online](#) for updates and enhancements.

Recent citations

- [Gyrokinetic modelling of light to heavy impurity transport in tokamaks](#)
K. Lim *et al*
- [Pedestal structure, stability and scalings in JET-ILW: the EUROfusion JET-ILW pedestal database](#)
L. Frassinetti *et al*
- [Core tungsten transport in WEST long pulse L-mode plasmas](#)
X. Yang *et al*



IOP | ebooks™

Bringing together innovative digital publishing with leading authors from the global scientific community.

Start exploring the collection—download the first chapter of every title for free.

Predictive multi-channel flux-driven modelling to optimise ICRH tungsten control and fusion performance in JET

F.J. Casson¹ , H. Patten² , C. Bourdelle³, S. Breton³, J. Citrin⁴, F. Koechl¹, M. Sertoli^{1,5}, C. Angioni⁵, Y. Baranov¹, R. Bilato⁵, E.A. Belli⁶, C.D. Challis¹, G. Corrigan¹, A. Czarnecka⁷ , O. Ficker⁸ , L. Frassinetti⁹ , L. Garzotti¹ , M. Goniche³, J.P. Graves² , T. Johnson⁹ , K. Kirov¹, P. Knight¹, E. Lerche^{1,10}, M. Mantsinen^{11,12}, J. Mylnar⁸, M. Valisa¹³ and JET contributors^a

*EUROfusion Consortium, JET, Culham Science Centre, Abingdon, United Kingdom of Great Britain and Northern Ireland

¹ UKAEA, Abingdon, United Kingdom of Great Britain and Northern Ireland

² EPFL-SPC, Lausanne, Switzerland

³ CEA, Saint-Paul-lez-Durance, France

⁴ DIFFER, Eindhoven, Netherlands

⁵ IPP, Garching, Germany

⁶ General Atomics, San Deigo, CA, United States of America

⁷ IPPLM, Warsaw, Poland

⁸ IPP-CAS, Prague, Czech Republic

⁹ KTH, Stockholm, Sweden

¹⁰ LPP-ERM/KMS, Brussels, Belgium

¹¹ Barcelona Supercomputing Center, Barcelona, Spain

¹² ICREA, Pg. ILluís Companys 23, 08010 Barcelona, Spain

¹³ RFX, Padova, Italy

E-mail: francis.casson@ukaea.uk

Received 11 December 2019, revised 3 March 2020

Accepted for publication 25 March 2020

Published 21 May 2020



CrossMark

Abstract

The evolution of the JET high performance hybrid scenario, including central accumulation of the tungsten (W) impurity, is reproduced with predictive multi-channel integrated modelling over multiple confinement times using first-principle based core transport models. Eight transport channels (T_i , T_e , j , n_D , n_{Be} , n_{Ni} , n_W , ω) are modelled predictively, with self-consistent sources, radiation and magnetic equilibrium, yielding a system with multiple non-linearities: This system can reproduce the observed radiative temperature collapse after several confinement times. W is transported inward by neoclassical convection driven by the main ion density gradients and enhanced by poloidal asymmetries due to centrifugal acceleration. The slow evolution of the bulk density profile sets the timescale for W accumulation. Modelling this phenomenon requires a turbulent transport model capable of accurately predicting particle and momentum transport (QualiKiz) and a neoclassical transport model including the effects of poloidal asymmetries (NEO) coupled to an integrated plasma simulator (JINTRAC). The modelling capability is applied to optimise the available actuators to prevent W accumulation, and to extrapolate in power and pulse length. Central NBI heating is preferred for high performance, but gives central deposition of particles and torque which increase the risk of W accumulation by increasing density peaking and poloidal asymmetry. The primary mechanism for ICRH to control W in JET is via its impact through turbulence in reducing main ion density peaking (which drives inward neoclassical convection), increased temperature screening and turbulent W diffusion. The anisotropy from ICRH also reduces

^a See Litaudon *et al* 2019 ([10.1088/1741-4326/aa5e28](https://doi.org/10.1088/1741-4326/aa5e28)) for the JET team.

poloidal asymmetry, but this effect is negligible in high rotation JET discharges. High power ICRH near the axis can sensitively mitigate against W accumulation, and dominant ion heating (e.g. He-3 minority) is predicted to provide more resilience to W accumulation than dominant electron heating (e.g. H minority) in the JET hybrid scenario. Extrapolation to DT plasmas finds 17.5 MW of fusion power and improved confinement compared to DD, due to reduced ion-electron energy exchange, and increased Ti/Te stabilisation of ITG instabilities. The turbulence reduction in DT increases density peaking and accelerates the arrival of W on axis; this may be mitigated by reducing the penetration of the beam particle source with an increased pedestal density.

Keywords: JET, integrated modelling, impurity transport, ICRH, isotope scaling, DT extrapolation, tungsten

(Some figures may appear in colour only in the online journal)

1. Introduction

The ‘hybrid’ scenario is one of two high performance H-mode scenarios developed in JET with the ITER-like wall for a future DT campaign [1]; it operates at a lower density and higher β compared to the alternative high current ‘baseline’ scenario. The goal for both DT scenarios is to produce 15 MW of fusion power for 5 s. To produce a steady high performance plasma, the hybrid scenario development must address three connected challenges: (i) to maintain divertor heat loads within acceptable limits, (ii) to control the accumulation of the radiative tungsten (W) impurity in the plasma core, and (iii) to avoid performance limiting MHD modes. The present work focuses on the hybrid scenario, since it is more prone to central W accumulation due to its stronger density peaking and the avoidance of sawteeth.

In this work, we use the word ‘accumulation’ to refer to the inward radial transport of impurities, which leads to their increasing concentration *near the magnetic axis*. The mechanism responsible for central W accumulation in JET is inward neoclassical convection driven by main ion density gradients and strongly enhanced by poloidal asymmetries due to rotation [2–4]. The neoclassical impurity convection dominates the phenomenology in high performance JET discharges, and is fundamental to the present work. It is instructive to recall from [3] the analytic formulation of the neoclassical impurity flux in the Pfirsch–Schlüter limit:

$$\frac{R\Gamma_Z^{neo}}{n_c} = q^2 D_c Z \left[\left(\frac{1}{Z} \frac{R}{L_{nZ}} - \frac{R}{L_{ni}} + \frac{1}{2} \frac{R}{L_{Ti}} \right) P_A - 0.33 P_B f_c \frac{R}{L_{Ti}} \right] \quad (1)$$

where Γ_Z is the flux of the impurity, R is the major radius, $L_n = -|\nabla n|/n$ is a gradient length-scale, f_c is the fraction of circulating particles, D_c is the classical diffusion coefficient, $\langle \cdot \rangle$ is the flux surface average, and P_A and P_B are two geometrical coefficients related to the poloidal asymmetry (with no asymmetry, $P_A = 1$ and $P_B = 0$, while in JET they can both reach values of order 100).

The slow timescale of main ion density evolution over multiple confinement times (tracked by the electron density in figure 1) sets the timescale for central W accumulation [2, 5]. Central NBI heating is the main actuator necessary for high performance in the hybrid scenario, but comes at the price of

central deposition of particles and torque which pose the risk of W accumulation [5]. Central ICRH has multiple beneficial effects which can mitigate this, including: (1) flattening the bulk plasma density and rotation profile through an increase in turbulence relative to the NBI source, (2) increasing turbulent diffusion of the tungsten impurity, (3) increasing the neoclassical temperature screening from both main ions and fast ions, enhancing the outward neoclassical W convection [6], and (4) reduction of tungsten poloidal asymmetry through the parallel force balance with an anisotropic minority, reducing the neoclassical convection [6, 7].

These various effects of ICRH on W create a space for potential optimisation, which is a challenge to predict, requiring both integrated flux-driven simulations and high-fidelity ICRH modelling. This work combines both these modelling elements to predict the optimal ICRH configuration for core W control in the JET hybrid scenario: section 2 describes a recently developed multi-channel flux-driven predictive capability for all core transport channels using first-principle based transport models. Section 3 presents the validation of this capability in reproducing the evolution of JET hybrid scenario DD plasmas over multiple confinement times, including the central W accumulation and associated central radiative collapse of electron temperature. Building on a first presentation of this capability for NBI only plasmas [5], the accuracy of W accumulation predictions are here refined, and extended to cases including ICRH. Section 4 introduces detailed standalone ICRH modelling, comparing three codes with different assumptions, and improves the fast ion anisotropy parametrisation (following [8]) to assess the impact of ICRH fast ions on neoclassical transport, improving the accuracy of previous work [6]. The ICRH modelling is also used to calibrate the correct power densities to be used in flux-driven integrated simulations. In section 5, the integrated modelling tools are applied to understand and optimise the available actuators of plasma heating to prevent W accumulation. In section 6, the modelling of the extrapolated maximum power DD scenario (with ICRH optimised for W resistance), is extended to DT and TT plasmas, investigating the combined impact of pedestal, current, and isotope scaling on both fusion performance and W accumulation. The modelling tools are used to guide the scenario development, assessing the potential to

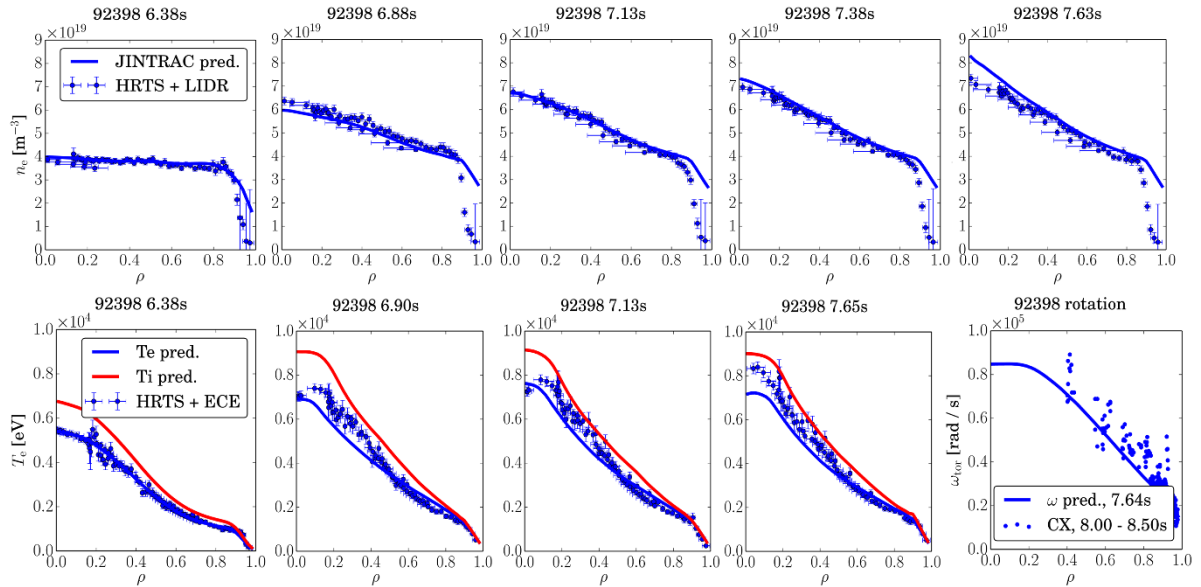


Figure 1. Evolution of predicted bulk plasma profiles in multi-channel JINTRAC-QuaLiKiz-NEO simulation compared to experimental measurements for JET 92398. The simulation is initialised at 6.38 s with profiles fitted from measurements just after the H mode and full NBI power are established (timetraces of the same simulation are shown in figure 2). After the initial condition, the core plasma is simulated fully self-consistently using experimental data only to determine the boundary conditions: Boundary conditions at the LCFS are constant in time, and pedestal top target values are constant after 6.9 s. Core T_i measurements are unavailable; neutron rate analysis supports $T_i \sim 1.25T_e$, which is used for the initial condition.

optimise and integrate both duration and fusion performance of the scenario.

2. Models and assumptions

An accurate predictive description of W accumulation requires a turbulent transport model capable of correctly predicting particle and momentum transport channels (in addition to the energy channels), and a neoclassical transport model which includes poloidal asymmetries due to the centrifugal force and fast ion anisotropies. For this work, these requirements have been met by coupling the drift kinetic neoclassical solver NEO [9–11] and the fast quasilinear gyrokinetic model QuaLiKiz [12, 13] to the integrated modelling suite JINTRAC [14, 15]. The integration of these transport models into JINTRAC allows eight (or more) transport channels T_i , T_e , j , n_D , n_{Be} , n_{Ni} , n_W , ω (angular frequency is denoted by ω), magnetic equilibrium, sources and radiation to all be evolved self-consistently.

In all cases, NEO is run including the effect of poloidal asymmetries on all species due to rotation (but the impact of anisotropic fast ions on asymmetry is included only in section 4). In the high torque, strongly rotating JET plasmas presented, the poloidal asymmetries increase core neoclassical W transport by a factor of $P_A \sim 90$. In all cases presented, the QuaLiKiz transport model is run with the inclusion of ExB shear from mid-radius outwards (shear rate set to 0 for $\rho > 0.5$), and with ITG, TEM and ETG scales included (indicated as most appropriate from previous validation studies [13, 67]), but without poloidal asymmetries (the impact of poloidal asymmetry on turbulent W transport is much less than on neoclassical transport [6]). The QuaLiKiz model is allowed

to run all the way up the axis, and instabilities are found up to $\rho > 0.1$ (e.g. figure 8(b)). The particle transport from QuaLiKiz and NEO (with a realistic impurity mix) is sufficient (even in the region close to the axis) to produce realistic bulk density profiles; no ad-hoc particle transport is required. An ad-hoc model is added to mimic the effect of electromagnetic stabilisation of the ITG instability, known to be significant in JET hybrid scenario [16, 17]: The ∇T_i inputs to QuaLiKiz are reduced by a factor of the local $\beta_{\text{thermal}}/\beta_{\text{total}}$, (between 0.7 and 1 in the reference discharge) shifting the ITG threshold and correcting the under-prediction of T_i otherwise observed in QuaLiKiz simulations of hybrid discharges [5, 13] (the factor used accounts for fast ion stabilisation, cross-correlated in JET with total β and EM stabilisation [18–20]). In the reference discharge presented in this paper, T_i measurements are unavailable, so we have validated the EM-stabilisation model on a similar hybrid discharge from the JET-C era, in which accurate T_i measurements are available; this validation is presented in appendix 1. More details of the NEO coupling are presented in appendix 2, and validation of the QuaLiKiz coupling is presented in [13].

NBI heating is simulated self-consistently with the PENCIL code [21]. For the reference discharge, the H minority ICRH is also simulated self-consistently with PION [22, 23], but in the later sensitivity and extrapolation studies, prescribed ICRH profiles are used (and compared with advanced models in section 4). In order to fix a constant minority concentration in PION, the ICRH minority is not included in the JETTO transport equations, and its impact on confinement and dilution is not modelled. The fixed boundary equilibrium is solved with ESCO [14]. The plasma is modelled from the last closed flux surface to the axis, using a fixed pedestal width with a continuous (averaged) ELM model which

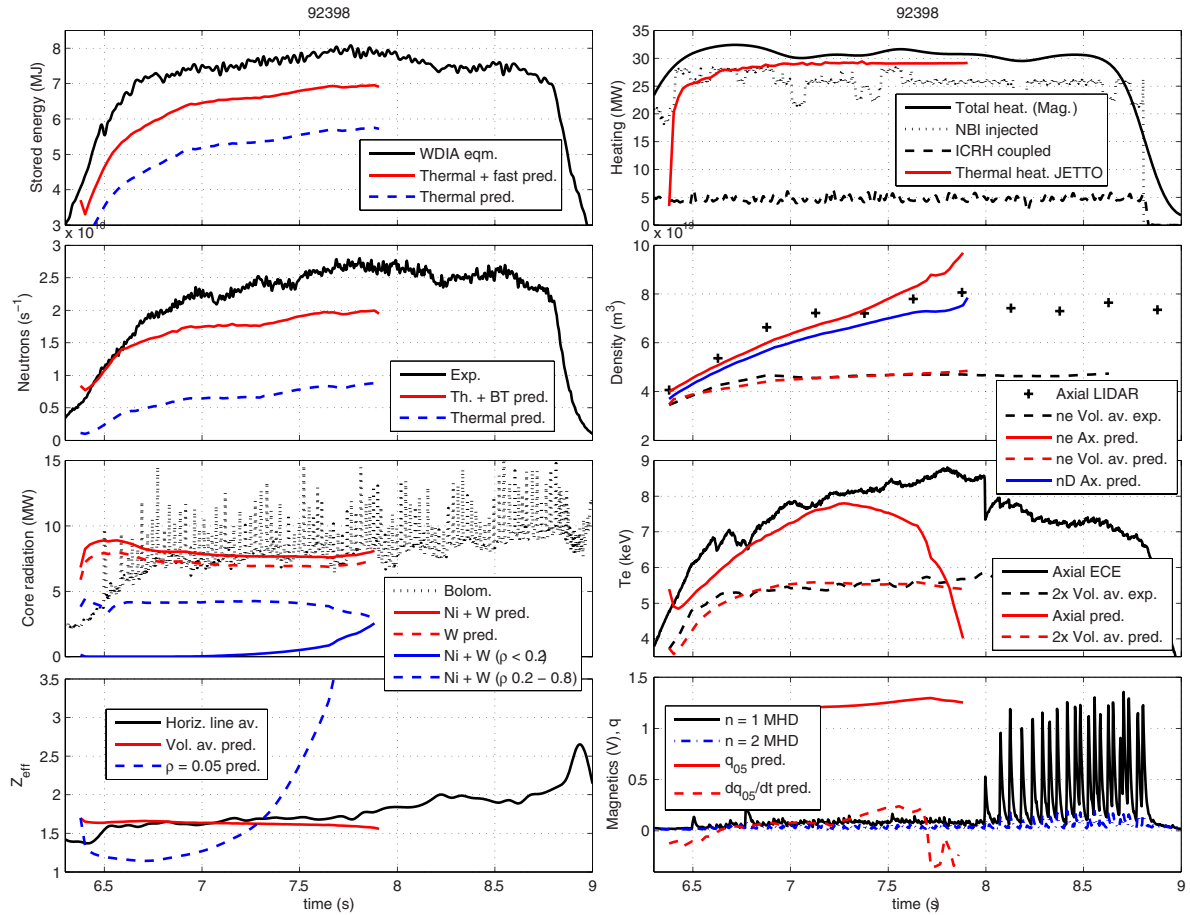


Figure 2. Evolution of global and axial quantities in JET 92398 compared with predictive multi-channel simulation with JINTRAC. Black curves are experimental data; coloured curves are simulated data. The safety factor at $\rho = 0.05$ is indicated by q_{05} . Thermal and beam-target neutron rates are predicted self-consistently (NBI + ICRH fast ion synergy is not included in the neutron rate).

adjusts anomalous pedestal transport in feedback control to a specified height target in each channel. The boundary conditions (from data) at the last closed flux surface (LCFS) are $T_i = T_e = 120$ eV, $n_D = 2.2 \times 10^{19} \text{ m}^{-3}$, $V_{\text{tor}} = 47 \text{ km s}^{-1}$ (low field side, LFS). The pedestal top density and temperature targets are taken from fits to experimental data, ramped gradually during the first 0.5 s following the experimental evolution, and constant thereafter ($T_e = 1500$ eV, $T_i = 1650$ eV, $n_e = 3.9 \times 10^{19} \text{ m}^{-3}$). The anomalous pedestal momentum transport is modelled from the ion transport by assuming Prandtl no. = 0.9. The SOL neutral source is modelled with the cold neutral model FRANTIC [24], also in feedback control, with a time-averaged particle source representing a $\sim 10\%$ fuelling efficiency from the gas puff. All charge states of the impurities Be, Ni and W are evolved with individual transport equations and atomic transitions, but only the average local charge is used to evaluate transport for each impurity. The impurity content is initialised in coronal equilibrium, and afterwards is free to evolve (boundary impurity flux, not density, is prescribed). ADAS data are used for ionisation, recombination and radiation. For W, an improved ADAS radiation model [25, 26] is used. No core MHD models are used, since the high performance phase of the hybrid scenario is free of sawteeth and tearing modes. Inside the pedestal top, the predictions depend

only on first-principle based models without adjustment of free parameters, with limited exceptions: (1) A minimum level of background transport is set at 3% of the standard Bohm-GyroBohm model [27]; this enhances numerical stability with a negligible influence on predictions. (2) Additional axial diffusion is prescribed in the electron temperature channel only: a Gaussian centred on the axis with a peak value of $0.1 \text{ m}^2/\text{s}$ and a standard deviation (SD) width of $\sigma = 0.075$ in ρ units, which aids numerical stability during W accumulation phases. (3) Since the EM stabilisation correction is ad-hoc, it effectively contains a free parameter in front of the ratio $\beta_{\text{thermal}}/\beta_{\text{total}}$ (set to 1 in all simulations and not adjusted to tune predictions).

3. Validation of predictive capability of scenario evolution

To validate the JINTRAC tool and the models and assumptions described in section 2, we simulate the evolution of the second highest performing hybrid pulse (#92398, $B_T = 2.8$ T, $I_p = 2.2$ MA, NB = 26 MW, ICRH = 4.5 MW, $H_{98} = 1.3$, $\tau_E = 0.17$ s) achieved in JET-ILW before 2019, from the start of the H-mode, until the accumulation of W on axis 1.6 s, $9\tau_E$ later (figures 1–3). The modelled density peaking

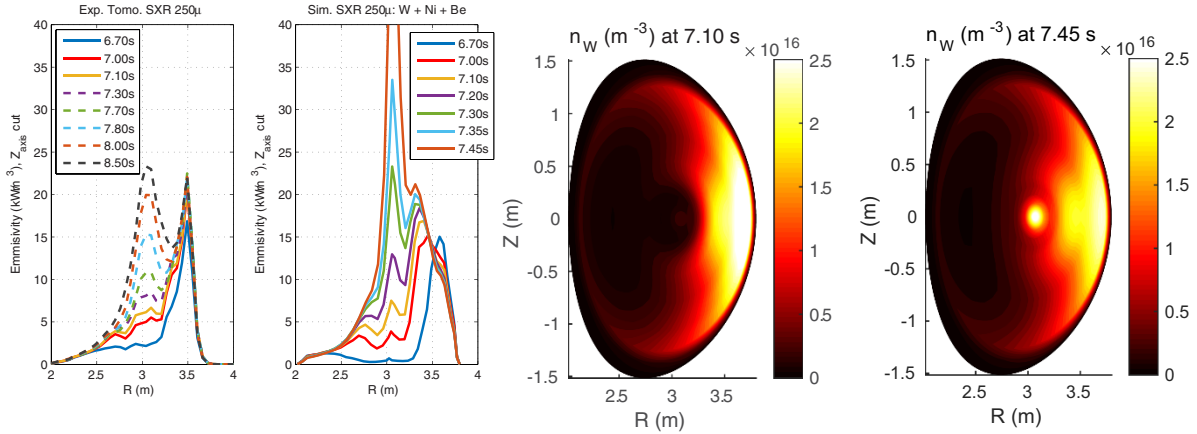


Figure 3. (1D profiles, left) Evolution of soft x-ray tomography for JET pulse 92398 compared to forward modelled SXR emission from W, Ni and Be in predictive simulation. The magnetic axis is at $R = 3.05$ m. Before central accumulation, W and Ni are localised on the LFS by rotation. The solid curves are at the same times in sim. and expt., the dashed curves indicate later times in expt. (2D profiles, right) Predicted W density before and after the start of central accumulation; Ni evolves similarly.

is extremely sensitive to T_i/T_e at the pedestal top [28]; larger values of T_i/T_e stabilise the ITG mode, T_i/T_e changes propagate inwards to the core, and the global stabilisation of the ITG can cause a large increase in density peaking. The pedestal top value $T_{i,ped}/T_{e,ped} = 1.1$, used in the presented simulations gives a density rise which very closely tracks the experiment (figure 1). Values of $0.9 > T_{i,ped}/T_{e,ped} > 1.3$ are all within experimental uncertainty. The electron temperature and rotation are also well predicted (figure 1). The three impurities are initialised as radially constant concentrations in coronal equilibrium with relative abundances 40:1:0.37 for Be:Ni:W, consistent with spectroscopic measurements, line integrated Z_{eff} , and total radiation. In the experiment, the total core radiation (dominated by W) is broadly constant during the high performance phase. In the simulation, the neoclassical pedestal impurity convection is inwards, and dominates diffusion, so there are no impurity losses. In order to avoid regions of zero impurity density, the impurity boundary influx is prescribed at $1e15/s$ (for all impurities), which results in less than 2% increase in total W content (and less for Be and Ni) over the simulation. In practice, no significant impurity source is required (after the simulation initial condition) to reproduce the measured level of radiation throughout the modelled phases, and the total impurity content is almost constant throughout the simulation. This indicates that the ELM flushing and inter-ELM W transport are in balance (no net influx through the pedestal over the ELM cycle) in this particular experiment (which maintains a constant ELM frequency with real time control), as also found in an NBI only pulse [5]. The same impurity and pedestal and assumptions are used in the later extrapolated cases.

The simulation reproduces well the global evolution into the high performance phase (figure 2), with some under-prediction of the total stored energy (14%) and neutron rate (24%). The profiles (figure 1) show that T_e is at most 5% under-predicted, which indicates that T_i or fast ion energy may also be slightly under-predicted. Simulations with TRANSP have shown up to 10% NBI-ICRH fast ion synergy in the neutron

rate in these conditions [29] (not present in these simulations) which may account for some of the shortfall in the predicted neutron rate.

After an initial phase of low field side centrifugal W localisation, neoclassical convection becomes inward and W starts to accumulate on axis from ~ 7.1 s onwards (figure 3). Qualitatively, this matches the soft x-ray observations, which show central radiation peaking from 7.3 s. Once significant W starts to accumulate, axial electron temperatures fall, in both simulation (7.2 s) and expt (7.7 s). In the simulation, once W accumulation begins, it quickly proceeds (faster than in the experiment) to an extreme accumulation leading to a radiative collapse of electron temperature on axis. This phase of the simulation is extremely sensitive, and ultimately becomes numerically unstable when radiation exceeds 2 MW in the small volume within $\rho < 0.2$. In the experiment, the W accumulation signals a drop in central electron temperature, and the end of the quiescent highest performance phase, but does not lead to the strong radiative collapse seen in the simulation. Instead, the maximum electron temperature is followed within 0.3 s by the arrival of $(m, n) = (1, 1)$ MHD activity (a single sawtooth, followed by fishbones) known to regulate W concentration on axis [30, 31]; no attempt is made to model this here (our goal is to understand the actuators of W accumulation). The modelling also reveals that before the W accumulation, the central safety factor is stable above 1, and supported by a large bootstrap current component. However, once the W accumulation is severe, a local loss of bootstrap current causes a drop in the central q ; suggesting that W accumulation could be causal in accelerating the arrival of MHD activity. The impact of MHD activity on W accumulation in JET has been widely reported [2, 25, 32], but this role of W accumulation as a sawtooth trigger has not been previously noted. Sawteeth provide one route to limiting high central concentrations of W, but are otherwise undesirable in the hybrid scenario ($\beta_N < 2.0$) because they can trigger performance degrading neoclassical tearing modes.

This section demonstrates that the modelling is capable of predicting complex multi-channel phenomenology on

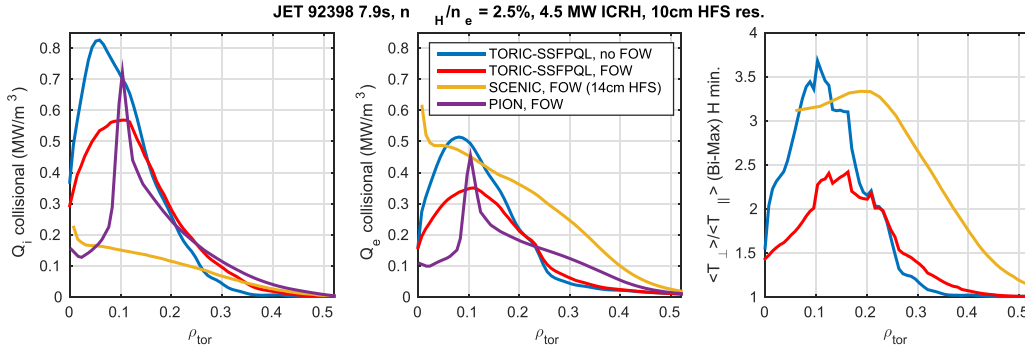


Figure 4. Comparison of SCENIC, TORIC-SSFPQL, and PION power deposition and minority anisotropy with a HFS resonance as in discharge 92398. The inclusion of FOW (approximate model) in SSFPQL reduces both power density and anisotropy. The minority anisotropy T_{\perp}/T_{\parallel} is here defined by the Bi-Maxwellian fit to the average energy moment over the flux surface for the total (thermal + fast) H minority distribution. PION (1D) finds $T_{\perp}/T_{\parallel} = 2.6$ at the ICRF resonance from the pitch angle averaged velocity distribution function using an ad-hoc formula obtained described in [23]. The PION estimate is in line with that given by TORIC-SSFPQL including FOW effects.

confinement timescales, and describes well the evolution of the scenario including the observed accumulation of W on axis. Both simulation and experiment demonstrate an increasing W concentration on axis, although the simulation exhibits a more sudden and extreme feedback during W accumulation. This suggest an additional transport process is acting in the experiment (most likely one which regulates main ion density peaking in the neoclassical core) which is not present in the simulation. Nevertheless, we conclude that the simulation qualitatively captures the main features and timescales of the scenario evolution until the phase where axial electron temperatures fall and MHD begins, and can be used to investigate the optimisation of heating system actuators for delaying the onset of W accumulation.

4. Fidelity of ICRH modelling and impact of ICRH minority anisotropy

In previous works [6, 33], we found that the ICRH fast ions could provide a potential avenue to optimise against W accumulation, but that these effects were very sensitive to details of the ICRH modelling: ICRH acts on neoclassical W transport, through the influence of fast ion anisotropy (acting to reduce W poloidal asymmetry and neoclassical convection) [6, 7, 33] and fast ion temperature screening [6, 33]. The previous works used TORIC-SSFPQL [34, 35] to compute the resonant minority distribution including its anisotropic pressure. For this work, a significant effort was made to improve the ICRH modelling and minority description, in order that the various effects of ICRH on W could be compared under the conditions relevant to high performance JET discharges. In order to understand the uncertainty in the ICRH modelling and its influence on the flux driven modelling, we present a comparison of power deposition and anisotropy for 92398, H minority heating for three ICRH codes with different assumptions (figure 4). Physical inputs were made identical as far as the codes allow but this *comparison* is not a code verification *benchmark*, since no attempt was made to reduce the models

to a common set of physics assumptions (which would give a benchmark with less experimental relevance). Instead, each code used the full physics it routinely supports.

The SCENIC package [36, 37], features a fast-wave solver and a coupled Monte Carlo Fokker-Planck solution including finite orbit widths (FOW) for the minority, a self-consistent shaped geometry with fast ion pressure, and a 3D Monte Carlo fast ion description. The TORIC-SSFPQL package features a 2D full-wave solver (TORIC) coupled to a Fokker-Planck continuum solution (SSFPQL) in a self-consistent closed loop coupling *for each species individually* in a general axisymmetric geometry. The PION code is a fast reduced model which features a wave field solution obtained with the superposition of two components of the wave field (in the limits of strong and weak absorption) based on the LION code, coupled to a 1D Fokker-Planck solver for the minority and majority species [22, 23], shown to be accurate for JET [38]. Both TORIC and SCENIC used a reduced mode spectrum ($n = \pm 27$) for computational efficiency (although they are capable of more), but PION used a full mode spectrum. All wave solutions include 2nd harmonic D direct absorption, but D beam ions are not included in the presented simulations (ICRH only, no NBI synergy). The fast D distribution is neglected in the SCENIC Fokker-Planck solver, but is included in both SSFPQL and PION. Both SCENIC and SSFPQL include magnetic trapping and the SSFPQL and PION results include an approximate model for FOW via an orbit broadening integral. Due to the self-consistent orbits and equilibrium in SCENIC, it was not possible to impose a fixed equilibrium identical to that used in PION and TORIC, and the minority concentration is not radially constant. Parameter scans in the SCENIC resonance location and minority concentration show that these minor differences in input are not a large cause of the differences between the results, the differences are rather due to the different physics assumptions in the models: The significant differences in the partition between ion and electron power absorption shown in figure 4 are most likely due to the absence of a non-thermal D population in the SCENIC Fokker-Planck solution (other differences in the model assumptions do not generate such

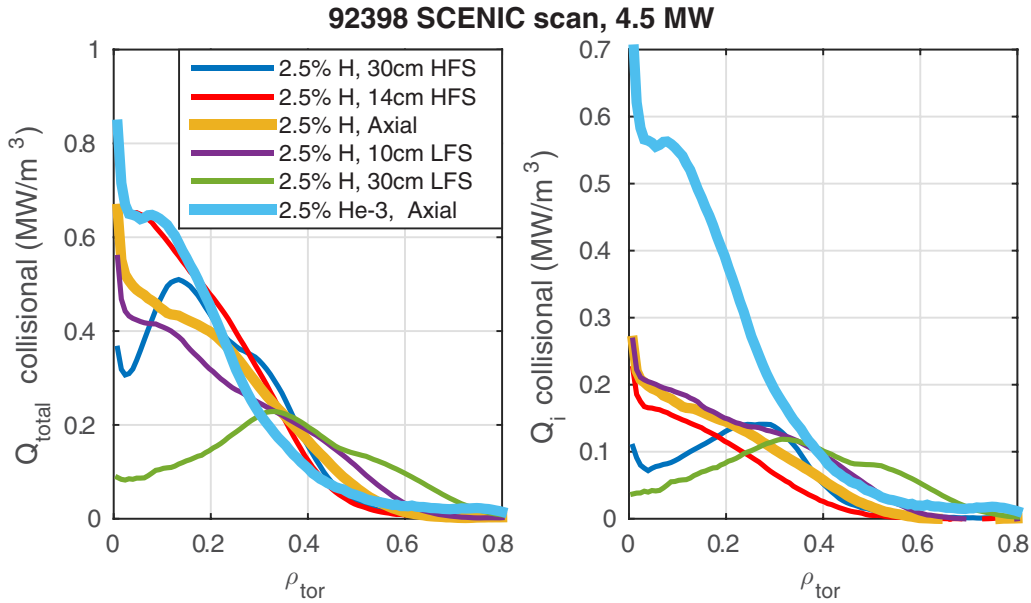


Figure 5. Scan of resonance locations and H vs He-3 minority heating with SCENIC, for the same conditions as figure 4. In all cases the total coupled power is 4.5 MW and $n = \pm 27$.

significant differences). The discrepancy shown here should motivate a detailed benchmark and analysis of the differences in power deposition including the nonlinear coupling of the wave solution and the Fokker–Planck solution, which is beyond the scope of this work.

Neither the trapping or FOW effects were used in previous W transport studies with TORIC–SSFPQL; the present TORIC–SSFPQL results show that the inclusion of these effects slightly reduce both power density and anisotropy compared to previous works [6]. The SSFPQL results indicate both a lower peak power density and anisotropy also with the inclusion of FOW effects (H minority anisotropy is correlated with direct absorption power density and collisional electron power density). The higher power fraction to electrons in SCENIC compensates any reduction in anisotropy from FOW effects. For the purposes of describing the minority distribution in order to investigate the effect of fast ions on neoclassical transport, we pass the SCENIC results to NEO, because they provide an upper bound on the anisotropy, and because the full minority velocity space distribution is provided in the form required to account for the differences between HFS and LFS resonances [8].

To support the integrated modelling, and to analyse fast ion effects on neoclassical W convection, we conduct a scan of resonance location and compare He-3 and H minority schemes with SCENIC, to assess the potential for ICRH optimisation (figure 5, and figures in appendix 3). The same simulation set is described in greater detail in [39]. The results verify the JET-ILW experimental findings that near-axial resonances produce the highest power densities when deposition is within ± 10 cm of the magnetic axis [40–43]. The He-3 minority yields a larger ion-heating fraction than H-minority as well as a slightly narrower collisional power deposition due to increased collisionality and reduced orbit widths.

To assess the impact of W asymmetry generated by the minority anisotropy in high-power JET hybrid scenario conditions, we use JETTO–NEO, interfaced to the SCENIC supra-thermal minority distribution. Unlike previous work [6, 33, 44], our treatment in this work now accounts for the weaker impact of HFS resonances described in [8]. The model in [8] (and described in appendix 3) nullifies the impact of anisotropy on W for HFS resonances, and reduces it for LFS resonances (for flux surfaces not tangent to the resonance at the LFS). To isolate the anisotropy, asymmetry and fast-ion effects on neoclassical W transport, JETTO cases are presented with *interpretive* bulk plasma profiles (including rotation) from 92398 at 48.63 s, when central accumulation is well advanced. W is evolved predictively to a steady state, with turbulent W diffusion given by the Bohm-GyroBohm model [27]. The Bohm-GyroBohm model is used (in this section only, for W transport only) because it does not have threshold behaviour of the first-principle based models, which only give appropriate transport levels if the bulk plasma channels which drive the turbulence are allowed to relax.¹⁴ W peaking in these JET conditions is determined by the combination of neoclassical convection with turbulent diffusion [2, 6]. Since the purpose here is to compare the impact of the minority on neoclassical convection, the Bohm-GyroBohm gives an acceptable estimate of the turbulent diffusion, and gives W peaking comparable to the experiment.

The SCENIC resonance scan in figure 5 is coupled to JETTO to predict W profiles (figure 6(a)) in the phase after W accumulation has begun. The quantity $P_A \sim V_{\nabla n, asym} / V_{\nabla n, sym}$ in equation (1) is the geometric ratio of the inward component

¹⁴ The method to predict a steady state in the present work differs method from that used in [2, 3, 6], where power balance was used to normalise the turbulent W transport from a gyrokinetic code. The latter may be more accurate but is not convenient within a predictive transport code.

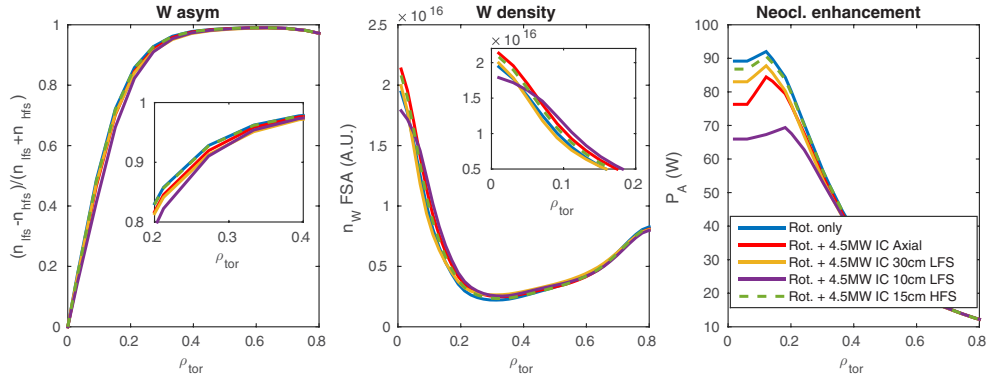


Figure 6a. Impact of anisotropy in ICRH resonance scan (2.5% H minority) on W poloidal asymmetry, predicted W profile, and neoclassical W transport enhancement due to poloidal asymmetry. Bulk plasma profiles including rotation are interpretive from 92398 at 8.63 s (bulk profiles as figure 1).

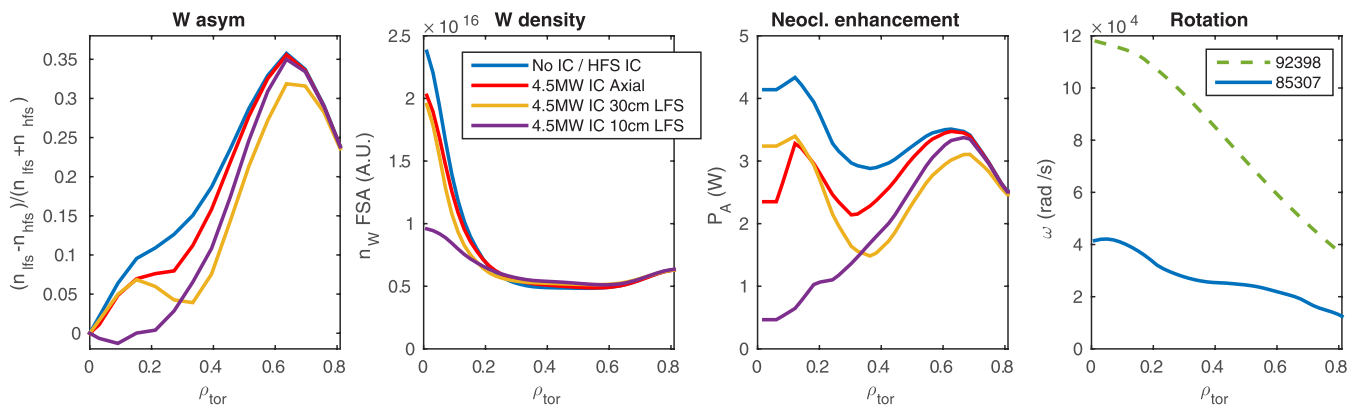


Figure 6b. Impact of anisotropy in ICRH resonance scan (2.5% H minority) on W poloidal asymmetry, predicted W profile, and neoclassical W transport enhancement, with reduced rotation from 85307. Other profiles are interpretive from 92398 at 8.63 s.

of neoclassical convection driven by main ion density peaking with and without the effects of poloidal asymmetry (discussed and defined in detail in [3, 6, 45]). The ICRH has most impact on the neoclassical transport and W profile when the resonance is ~ 10 cm on the LFS, but even then, the impact on the W asymmetry and predicted W profile is negligible. Even if the coupled power is increased to 8 MW (the maximum achievable in JET), the impact of the ICRH anisotropy on neoclassical W transport is insignificant. With SCENIC, we have also checked the impact of anisotropy in He-3 minority cases and found it to be negligible (at the same power, the fast minority temperature anisotropy is similar, but the fast minority density and pressure anisotropy is ~ 4 times smaller than with H minority). Varying the minority concentration between 1% and 4% for both H and He-3 minority also does not change the conclusions above.

The results in (figure 6(a)) must be compared with the results in [6], in which 4 MW of ICRH was shown to have a *large* impact on the predicted W profile in JET pulse 85307, via its influence on the W asymmetry and neoclassical convection. We have confirmed that the more complete description of the minority in the present work (using SCENIC and a more accurate parametrisation of the minority distribution, appendix 3) is *not* the main cause of the lesser impact of anisotropy even for LFS resonances in the present work. Instead,

the difference comes primarily from the different plasma conditions; 92398 has a much larger rotation, due to lower density and larger beam power (26 MW in 92398, 15 MW in 85307). This is verified (figure 6(b)) by replacing the rotation profile with that from 85307 used in [6]. Since rotational asymmetry scales with the square of the Mach number, P_A from rotation reaches ~ 90 in 92398, but only ~ 10 in 85307 [6]. In absolute terms, the impact of ICRH in reducing asymmetry and P_A is similar, but in relative terms is negligible in 92398. In high NBI power, highly rotating JET discharges, the ICRH anisotropy cannot compete with the extreme W asymmetry arising from rotation.

With lower rotation (in figure 6(b)), it becomes clear that our improved ICRH parametrisation (appendix 3) introduces a large sensitivity of the anisotropy effect on neoclassical convection to the IC resonance location, and that the optimum location for maximising this effect is slightly off axis (~ 10 cm) on the LFS, consistent with experimental results [43]. If the resonance is moved too far from the axis, the power density and consequent anisotropic pressure are not large enough to impact the predicted W profile (figure 6). If the resonance is on the HFS, only passing minority ions are heated anisotropically and the pressure anisotropy is less, resulting in a negligible impact of the minority on W asymmetry (figures 6 and 8 in [8]). The actual 92398 experiment had a resonance slightly

on the HFS (~ 10 cm), so the minority anisotropy effects are appropriately neglected in the validation of the multi-channel prediction presented in section 3.

Ref [6] also showed an enhancement to neoclassical temperature screening arising from fast ion temperature gradients. These effects are also included in the simulations in this section, but are even less significant than the effects of anisotropic pressure (in figure 6(a), compare the green dashed curve, where fast ion temperature screening is present, with the solid blue curve, where it is not; the anisotropy effect is absent in both these curves). In this case, the switch to the SCENIC model *is* responsible, since the inclusion of finite orbit width effects reduces the fast ion temperature gradients. This result is consistent with [46], which found a negligible impact of fast ion temperature screening with FOW effects, and [33, 44], which found that the impact of fast ions on W transport was likely exaggerated when using the earlier version of TORIC-SSFPQL (which did not include FOW effects) to provide fast ion inputs to NEO.

To summarise this section: Compared to previous works [6, 33, 44], we have refined our ICRH modelling and investigated in detail the effect of ICRH fast ions on neoclassical W transport. Fast ion enhancements to neoclassical temperature screening are found negligible, when finite orbit width effects are included. The anisotropy of ICRH fast ions, acting through parallel force balance, can push heavy impurities towards the HFS and counteract (some of) the impact of the centrifugal force. We have shown the anisotropy effect to be maximal for a resonance slightly on the LFS, and can be significant in plasmas with lower NBI induced Mach numbers. However, in the highest performance JET discharges, the anisotropic pressure is overwhelmed by large rotation driven asymmetries (W remains strongly localised on the LFS), and ICRH anisotropy does not present a significant actuator to optimise against W accumulation in these JET plasmas. The simulations presented in this section do not include the effect of the deposited ICRH power in driving turbulence and modifying the bulk profiles; which we will demonstrate are more significant. These effects are investigated and optimised in the next section, using fully predictive multi-channel modelling.

5. Optimisation of heating against W accumulation

We next apply the multi-channel predictive capability to predict future JET hybrid experiments, to support scenario development to optimise the heating actuators against W accumulation. The 2019/20 DD campaign on JET plans to increase NBI power to the full rated capacity of 32 MW, and to test and optimise different ICRH schemes within the hybrid scenario. In the flux-driven modelling in this and the following sections (unlike the sections above), we model ICRH using prescribed idealised Gaussian ICRH profiles with prescribed ion/electron heating fractions, to allow a systematic study separating the effects of ion/electron heating fraction from power density. The effects of anisotropy are now omitted, since they were shown in section 4 to be negligible in these conditions.

First, we investigate the impact of increasing the NBI heating on W (figure 7). In the 2019/20 campaigns, the beam power

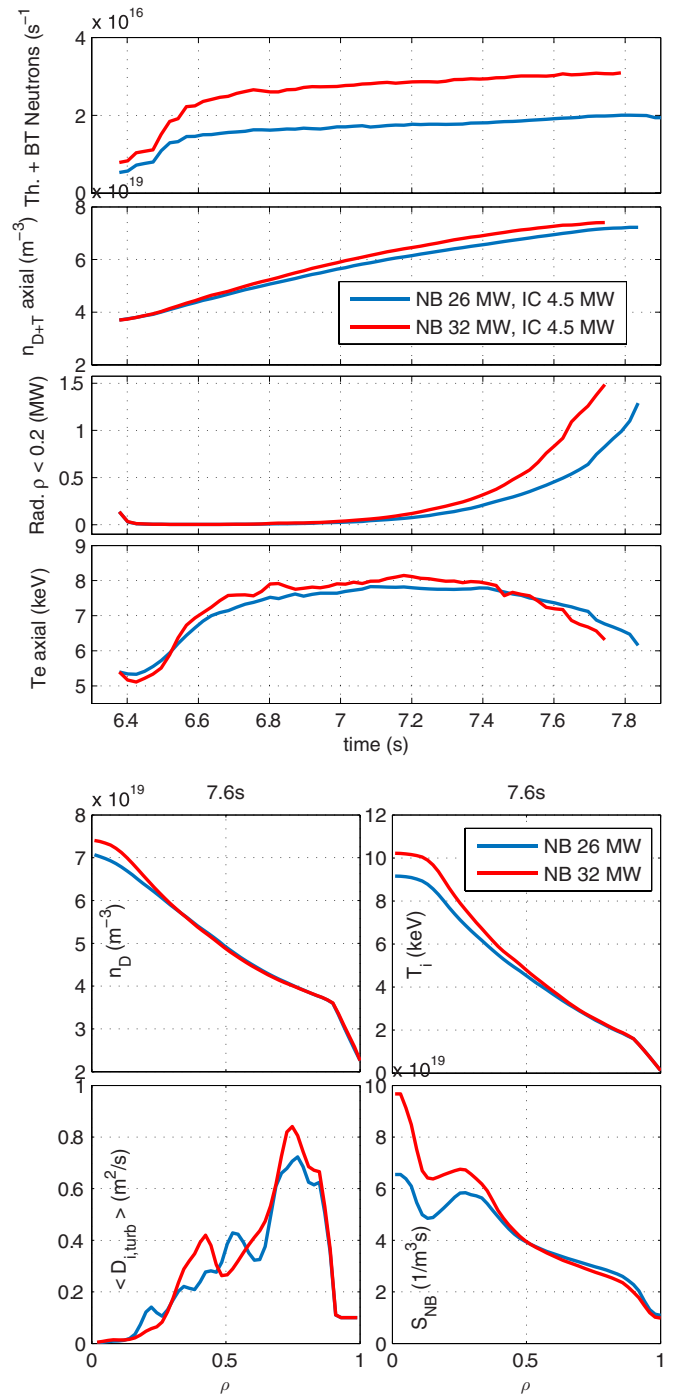


Figure 7. Impact of NB power (increasing beam voltage from 106 keV to 125 keV) on timing of W accumulation in predictive simulation. The turbulent diffusivity is averaged over 1 s preceding the kinetic profile time and is an effective diffusivity (includes turbulent convection). In these simulation the ICRH is the wide Gaussian on axis, 50% to ions, 50% to electrons.

will be increased by increasing the beam voltage to the maximum 125 keV. The results show that the increased beam penetration and central particle deposition increases both central density peaking and ion temperature peaking. The former slightly dominates the impact on neoclassical convection, and consequently the W accumulates slightly earlier.

Next, we investigate the impact of ICRH power and power density, scanning the total input power and the width of the ICRH deposition (figure 8(a)). The simulations in (figure 8(a)) use idealised IC heating, prescribed as a Gaussian centred on axis with a SD width of $\sigma = 0.14$ (ax, narrow) $\sigma = 0.21$ (ax, med), or $\sigma = 0.28$ (ax, wide) in ρ units. The ICRH collisional power deposition is 50:50 to ions:electrons, typical of H minority with 2nd harmonic D absorption. The power densities of the narrow (medium) deposition agree approximately with the TORIC (SCENIC) results for 2.5% hydrogen minority in figure 4, when scaled to the same coupled power. The benefit of central ICRH is demonstrated in the power scan; increasing central RF power drives central ITG turbulence, which increases effective D particle diffusivity, delaying the main ion density rise and also increasing turbulent W diffusion. The ion temperature peaking is also increased by ICRH, leading to larger neoclassical temperature screening.

With the wide ICRH absorption, 8 MW of localised ICRH power (the maximum foreseen for next JET campaigns) delays the W accumulation by only 0.25 s (here defined as the time when radiation with $\rho > 0.2$ exceeds 1 MW). In contrast, the scan of the deposition width at 8 MW shows a strong sensitivity to the power density deposited on axis. 8 MW deposited with the narrow deposition around the axis is far more effective, delaying W accumulation on axis by up to 1.5 s. With localised deposition on axis, the turbulent diffusion extends further towards the axis, reducing density peaking, and temperature screening is further enhanced by the central T_i peaking resulting from high power density in the neoclassical core. Scans of resonance location (not shown) demonstrate the same sensitivity to axial power density: To prevent axial W accumulation, ICRH power must be narrowly focused on the turbulence-free region near the axis, where the absence of turbulent diffusion can lead to extreme impurity gradients. ICRH schemes which favor narrow power deposition (via antenna phasing or narrower fast particle orbits) should therefore be favoured (studying this ICRH scheme optimisation is beyond the scope of this work). We note that the He-3 SCENIC results in section 4 have slightly narrower power deposition compared to the H minority scheme, due to the narrower fast ion orbits.

Next, we compare the effects of electron vs ion heating schemes with the same *total* power density for controlling W accumulation (figure 8(b)), an optimisation which is not *a priori* obvious, or known from JET experiments [40, 42]. The simulations make a clear prediction, as yet untested for the JET hybrid scenario: ion heating schemes should delay the arrival of W on axis. For localised axial deposition (narrow Gaussian), going from 50% ion heating (typical of H minority) to 80% ion heating (typical of He-3 minority) could delay W accumulation by more than 1 s. The ion heating increases effective turbulent diffusion in the region $\rho = 0.2 - 0.4$, reducing density peaking [47]. In the neoclassical core $\rho > 0.2$, the ion temperature peaking and W screening is strongly enhanced by the ion heating.

We stress that the predicted benefits of ion heating are *specific to this JET scenario*, with decoupled ions and electrons, $T_i < T_e$, dominant ITG turbulence for the particle transport,

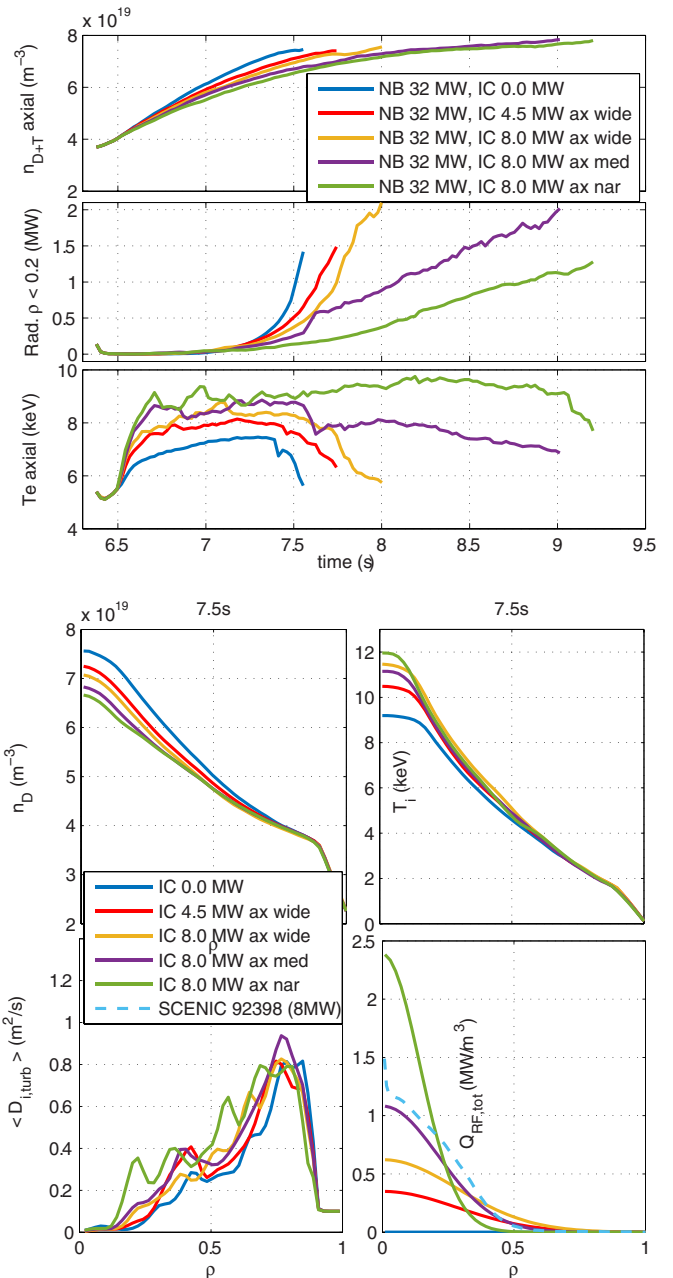


Figure 8a. Impact of IC heating (H-minority like) power and deposition width on timing of W accumulation in predictive simulation. For comparison of the ICRH power density, The SCENIC results (dashed line) are the 14 cm HFS 2.5% H case from figure 5, scaled up to 8 MW.

dominant neoclassical convection for W, and heating localised on axis in the region where neoclassical transport dominates. Electron heating allows the discharge to tolerate higher levels of W on axis before a radiative collapse, but the ion heating instead delays W accumulation, acting on the bulk profiles (reducing density peaking and increasing temperature peaking) to reduce the inward neoclassical impurity convection. These results are not relevant to ITER, where rotation and neoclassical W transport will be less significant, and ion-electron coupling will be greater.

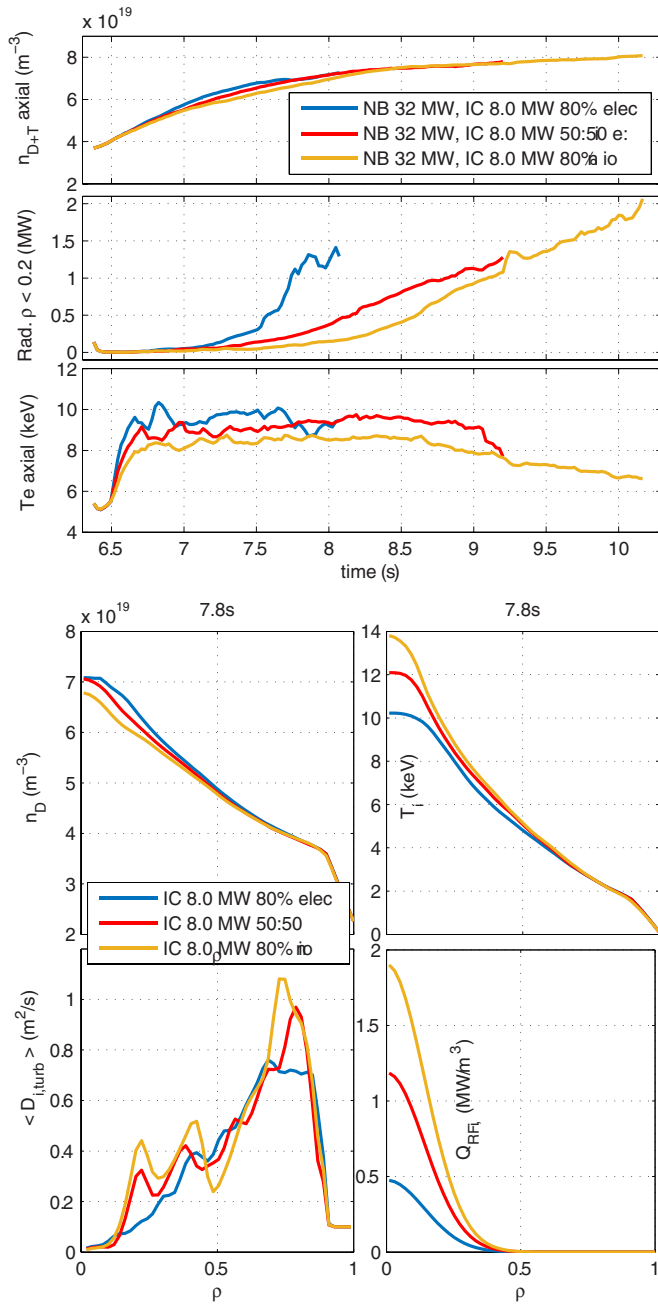


Figure 8b. Impact of ion vs electron IC heating on timing of W accumulation in predictive DD simulation at maximum JET power. These simulations all have 32 MW NB with 8 MW idealised IC heating prescribed as a narrow Gaussian centred on axis.

The present prediction is in contrast to a recent experiment in AUG [33], which found that ECRH was more beneficial than ICRH (~50:50 ion:electron) in preventing W accumulation. Compared to the JET hybrid pulse modelled here, the AUG plasmas had lower Mach number and higher RF power density, increasing the contribution of turbulent W transport (which may also be less strongly dominated by ITG in AUG). The AUG plasmas also had weaker i-e coupling and 1,1 MHD activity before W accumulation. Previous experiments in JET-C [40] also suggested that electron heating

schemes are more effective in preventing Nickel accumulation (also in lower rotation conditions).

The apparent discrepancy between our modelling and these experiments deserves discussion: In our simulations (with no MHD activity), the beneficial effect of centrally localised ion heating results from optimising the profiles for the central neoclassical transport. In the analysis of [33, 40], the impact of less localised heating on turbulent transport is interpreted as significant, and central MHD also complicates the comparison. In both experiments, it is challenging to separate the impact of different heat deposition *profiles* from different ion-electron heating *fractions*, in contrast to our present simulations where the heating fraction is varied with a fixed axially local deposition profile. In [40], the electron heating scheme is very much off-axis. In [48], it was shown that turbulent W diffusion is maximised at comparable electron and ion heat fluxes; we have verified that QuaLiKiz qualitatively reproduces this result, but in the flux driven integrated modelling it is insufficient to overcome the stronger effects of neoclassical transport through variation of the main ion profiles (this is true also at lower rotation and more extreme electron heating). To close this discrepancy, future work should i) verify QuaLiKiz W transport (with collisions) in mixed ITG/TEM regimes against full gyrokinetics, and against the study of turbulent convection in [49], where the treatment of subdominant TEM modes is significant, ii) Attempt to reproduce to the AUG experiments [33] with flux-driven integrated modelling, iii) Examine experimentally the effectiveness of He-3 and H-minority heating schemes with comparable resonance location and power deposition in MHD-free conditions (such experiments are planned in JET).

In the simulations presented in this section and the following sections, the effects of ICRH fast ions have not been included, since (as demonstrated in section 4), their impact on neoclassical W transport via poloidal asymmetry and fast ion temperature screening is found to be small in the high rotation conditions modelled here. However, we have attempted multi-channel predictive simulations in which the ICRH fast ions were included in NEO (not shown), which demonstrated an increase in *main ion* neoclassical diffusion leading to locally decreased main ion density peaking and slightly delayed W accumulation (up to 0.5 s). This effect is as-yet unexplored in theory, and deserves further attention in a future study. It is not appropriate to include it within the integrated modelling here until it is better understood in a standalone investigation (a large velocity space resolution is required for proper quantification).

The modelling in this section shows that maximising ICRH power density on axis can delay W accumulation. These results qualitatively reproduce and explain experimental observations in JET-ILW [41, 43], demonstrating the predictive capability of our modelling with respect to the impact of ICRH on W accumulation. In addition, our simulations predict that ion heating schemes may further delay W accumulation in high power JET hybrid scenario conditions, if such schemes allow sufficient power to be coupled coupled with a narrow central deposition.

6. Extrapolation to DT

Next we apply the predictive tool to examine the impact of isotope on fusion performance and W accumulation. The maximum power DD extrapolations are compared to full tritium plasmas (TT) and DT plasmas (figure 9) with α heating. The DT plasmas are initialised with 50:50 isotope mix, and equal boundary densities ($n_D = n_T = 1.1 \times 10^{19} \text{ m}^{-3}$). The pedestal feedback controllers give identical transport and total neutral source to each isotope, and neutral penetration is consistent with isotope mass. The beam sources are configured as they will be in a DT campaign, with one beam box in T and one in D, with the expected energies and energy fractions. The different beam configurations for the isotopes gives deeper penetration of the D beam ($S_{T,ax}/S_{D,ax} = 0.8$ and $S_{T,\rho=0.8}/S_{D,\rho=0.8} = 1.3$) but near identical total beam fuelling for each isotope. The fast isotope mixing [50] means that the D:T ratio remains between 53:47 and 50:50 at all locations and times within the simulation. In DT cases, α particle heating is computed following [51]. 8 MW ICRH is prescribed, using the best-case narrow Gaussian (80% to ions) found most effective (in section 5) at delaying W accumulation and raising T_i . In this section, the DT predictions are conservative for the pedestal, since they include no pedestal scaling with power or isotope (the power scaling is added in section 6.1). Since the dilution due to the ICRH minority is not included, we overestimate the fusion yield by $\sim (1 - X)^2$, where $X = n_{\text{min}}/n_{D+T}$ is the minority concentration.

The isotope extrapolation with a fixed pedestal (figures 9 and 10) shows a positive effect on confinement with heavier isotope, due to the inverse ion mass scaling of the ion-electron energy exchange [52] and its interaction with the turbulent transport: In all cases, T_e is similar due to the stiffness of the ETG scale transport. In heavier isotopes, the transfer of energy from ions to electrons is less efficient, allowing to a larger T_i/T_e to be sustained, known to suppress the ITG instability (the collisional detrapping of trapped electrons ($\sim \nu_{ie}/\omega$) is also more effective at larger mass, reducing trapped electron mode drive [49, 53, 54]). The resulting enhancement in fusion performance in DT is 37%: At 9.5 s, the DD case has a DT equivalent fusion power [55] of 10.8 MW (computed using the DD_{eq} ratios defined in figure 10, at 9.5 s), while the DT case has a predicted fusion power of 14.8 MW (before limiting W accumulation in either case), with $\sim 50\%$ thermonuclear reactions and $\sim 50\%$ beam-target. In our simulation, the fusion power continues to rise after the central electron temperature becomes hollow (occurs when $T_{e,axial} < 7 \text{ keV}$, at 9.9 s in DT + α case). In experiment, it is unclear if the high performance phase could continue once the electron temperature becomes centrally hollow (figure 9, inset), or if performance limiting MHD would be triggered.

To highlight the role of ETG scale transport in the prediction of positive isotope scaling, we have repeated the isotope scan with ETG scale transport removed, and also without ExB shear acting in the turbulent transport model (figure 10). While

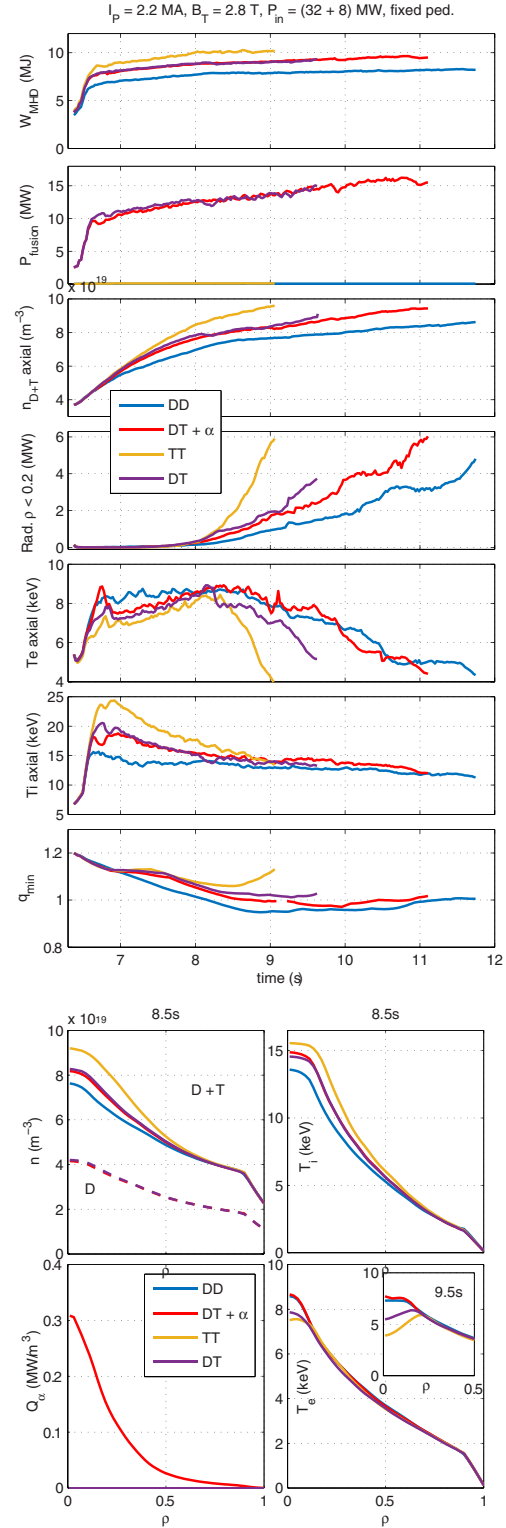


Figure 9. Impact of isotope and α heating on fusion performance and timing of W accumulation in extrapolations of 92398 to the maximum JET heating power (fixed 92398 pedestal). These simulations all have idealised IC heating with 8 MW coupled as a narrow Gaussian centred on axis, with 80% delivered to the ions. The NBI power coupled to the plasma is $P_{\text{NB,DD}} = 30.7 \text{ MW}$, $P_{\text{NB,DT}} = 32.4 \text{ MW}$, $P_{\text{NB,TT}} = 33.9 \text{ MW}$; small differences in NBI power are due to operational limitations in different isotopes.

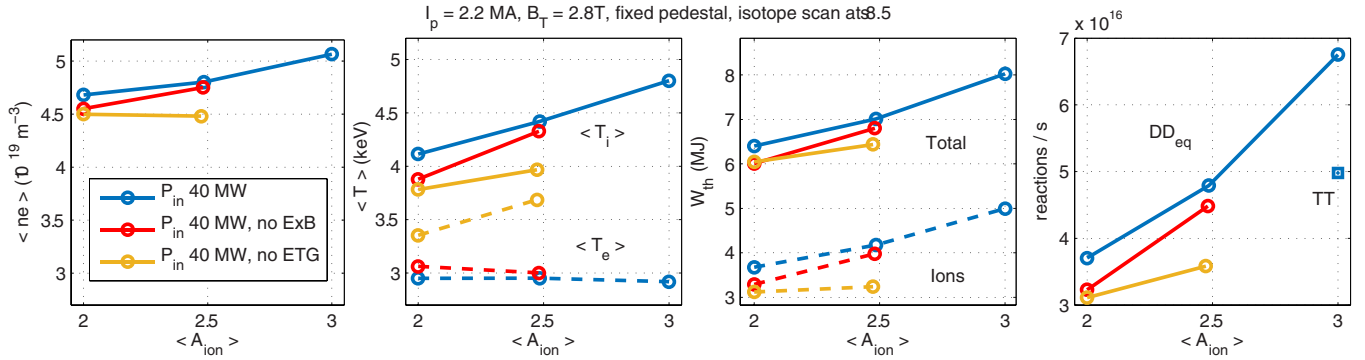


Figure 10. Predicted isotope scaling of core thermal stored energy and performance (fixed pedestal, fixed input power) with and without ETG scales and ExB shear at $t_{NBI} + 2.2$ s. Energy and temperatures are volume averaged. DD_{eq} indicates the DD equivalent neutron rate of a DT or TT plasma, used to compare fusion performance across isotopes: In TT plasma, $R_{DD,eq} = R_{TT}\{TT\} \cdot R_{DD}\{DT\} / R_{TT}\{DT\}$ where $R_{TT}\{DT\}$ indicates the volume integrated rate of TT reactions in the DT plasma, used to adjust for the difference in cross sections between DT and DD reactions. In DT plasma, $R_{DD,eq} = R_{DD}([n_T + n_D]/n_T)^2$, where $\langle \rangle$ is the volume average.

the total stored energy scales positively with isotope in all cases, the scaling of ion temperature and fusion performance with isotope is much stronger in the cases *with* ETG. The cases *without* ETG show a consistently lower T_i/T_e , leading to less efficient suppression of ITG transport and *lower* overall performance. Without ETG, the positive isotope scaling of stored energy is only in the electrons, and does not lead to any increase in fusion performance. Comparing the cases with and without ExB shear, we see that although ExB does modestly increase performance as expected, the impact is similar in both isotopes, and is not responsible for the positive isotope scaling. Although beams and rotation are both modelled self consistently, the predicted rotation profiles in DD, DT and TT are very close, with negligible differences in the (dimensional) ExB shear rate.

Inspection of the channels through which power is lost (table 1), further demonstrates the role of electron scales: Comparing cases with and without ETG, we see significant differences in power lost through the electron channel. In cases with ETG, the electron channel carries 32% in DD (40% in DT) of the power loss. In cases with only ion scales, the electron channel carries only half as much, 15% in DD (20% in DT). The slightly higher heating in DT cases (due to beam configuration and alpha heating), is carried mostly by the electron channel in cases both with and without ETG scales, with no increase in electron temperature. Without the ETG scale, the extra heating in DT is carried by the electron channel, with slightly larger electron temperature gradients required to accommodate this additional heat flux.

The mechanism of this positive isotope scaling is a complex interplay between transport effects (including EM stabilisation, T_i/T_e , ν_{ie}/ω , and ETG scales) and collisional energy exchange. In the modelling, this regime can only be accessed due to the EM suppression of the ITG, which increases $T_i > T_e$, bringing the plasma into a domain where both ETG transport and the energy exchange term become relevant. The decrease in the efficiency of the energy exchange term with heavier isotope allows a larger T_i/T_e to be sustained, which in turn suppresses ITG transport further (but only in simulations

Table 1. Power lost via ion, electron and radiation channels, integrated from the axis to $\rho = 0.8$ and time averaged from 8.0–9.0 s ($t_{NBI} + 1.7$ – 2.7 s) for the cases in figure 10. The loss power balances the total heating within 0.6 MW; the scenario is not a perfect steady state.

Case	P_i (MW) loss	P_e (MW) loss	P_{rad} (MW) loss	P_{aux} (MW) heating	P_α (MW) heating
DD	17.8	10.8	5.0	34.3	0.0
DT	18.0	14.8	5.3	35.5	2.2
DD, no ETG	23.2	5.7	4.6	34.0	0.0
DT, no ETG	25.0	7.3	4.3	35.1	1.6
DT, no α	17.1	12.3	5.4	35.5	0.0

with ETG scales included). We note that the self-consistent beam fast ion content in our DT simulations is up to 20% larger than in DD, due to the slower slowing down time, but the EM stabilisation factor is similar in DD and DT, since the fast ion energy density scales similarly to the thermal stored energy. The EM stabilisation factor is therefore not the *direct* cause of the positive isotope scaling but is important in accessing the regime where the ETG scales and collisional energy exchange are relevant.

Some words of caution on this prediction of isotope scaling (specific to cases with $T_i > T_e$) are in order: Very few multi-scale validations of non-linear gyrokinetic transport models exist in mixed ITG/ETG regimes [56–58], and none in these conditions, with $T_i > T_e$. In addition, the QuaLiKiz model includes only a simple model for cross scale interaction in its saturation rule. Furthermore, the electromagnetic stabilisation on the ITG is a crucial element in accessing this regime and is treated in an ad-hoc way in our modelling (appendix 1). As outlined above, the predictions shown here depend on the interaction of channels that can only be found with flux driven profile modelling combined with several effects at the forefront of the understanding of turbulence.

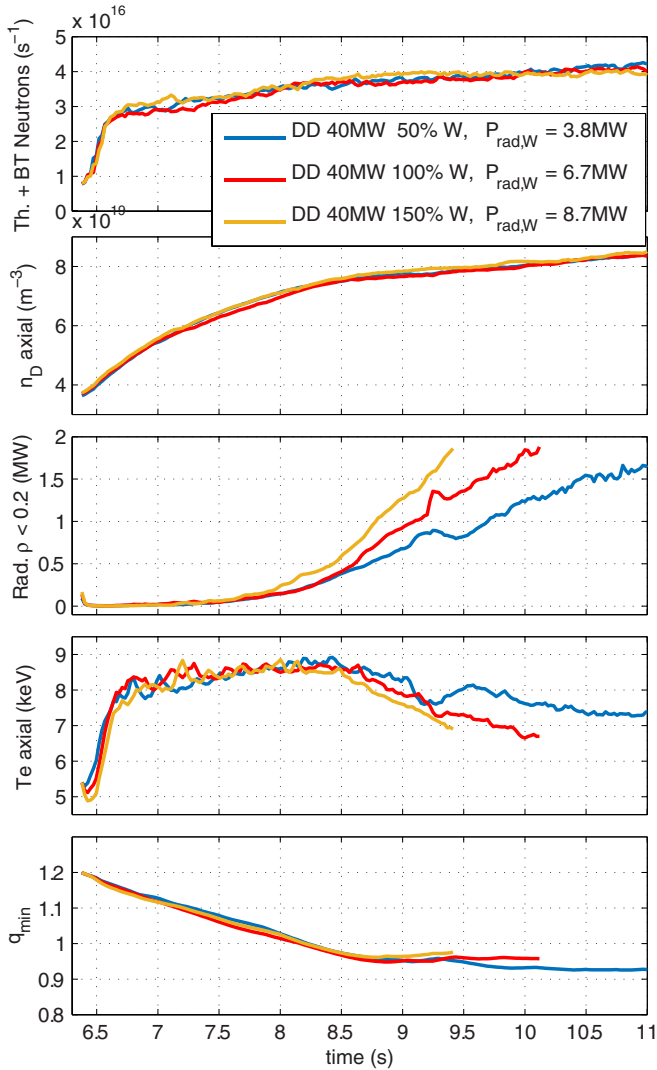


Figure 10a. Impact of varying the total W concentration (source) on scenario evolution for the DD case with 32 MW NBI and 8 MW ICRH (80% ions) and fixed pedestal. 100% W indicates the concentration used in all other simulations, chosen to match total P_{rad} for 92398 with 30 MW input power (as shown in figure 1).

These predictions motivate further study with non-linear multi-scale turbulence in these conditions, and a focus on improving and verifying quasilinear transport models with respect to electromagnetic stabilisation and multi-scale interactions. Experimental data on isotope scaling in these high power conditions is also rare, but new experiments are planned in future TT and DT campaigns in JET. The isotope transport scaling in lower power plasmas (with $T_i = T_e$) is also not fully captured by the present quasilinear models [59, 60]; improving the quasilinear description of the effects described in [54, 61, 62] could further improve predicted confinement in tritium.

Unfortunately, the improved confinement in tritium also leads to additional density peaking, and consequently, earlier W accumulation (figure 9). One possible solution to extend the duration of the hybrid scenario (explored in section 6.1) would be to increase density at the pedestal top (either by an increased triangularity, plasma current, or an increase with

heavier isotopes [59]), giving less central beam deposition and a slower timescale for density peaking. The simulations in figure 10 also show that in long DT pulses, q_{min} drops below 1 after about 2.5 s of evolution (before the W accumulation), which indicates that the duration of pulse may be limited by $(m,n) = (1,1)$ MHD (not included in our simulation) triggering performance limiting tearing modes. The impact of extrapolation of the current and pedestal on current diffusion is explored in section 6.1.

We also compare DT simulations with and without α heating (figure 9) and found it makes only minor differences to scenario performance or the timing of the W accumulation; since the ETG scales give very stiff electron transport, stored energy is insensitive to electron heating (or radiation): The inclusion of α heating increases axial electron temperature by only $\sim 5\%$, localised only in the core neoclassical region. There is negligible impact of α heating on the turbulent transport (α particles are not included as a species in the transport model). The main impact of the α heating is that it can compensate electron energy lost through radiation, and can therefore delay radiative collapse, giving a similar benefit and power densities as ICRH primarily to the electrons (see section 5).

Increasing power and isotope mass are also expected to increase the source of W from divertor sputtering. To test the impact of this on the scenario, we have performed simulations with a 50% variation in the total initial W content, giving up to 10 MW total radiation with 8.7 MW W radiation (figure 10(a)). The results show the scenario performance is initially insensitive to the increase in the electron heat sink (up until radiative collapse), due to the stiffness of the electron heat channel. This result is in contrast to [5], which reported *increased* performance with increased radiation due to increasing T_i/T_e ; our simulations in the present work now include ETG turbulence (unlike [5]), and do not find increased performance with increasing radiation. However once W accumulation begins, the simulations with the higher W content unsurprisingly have an earlier radiative collapse, so control of the W source is important to build a robust scenario with steady performance.

6.1. Current, field and pedestal extrapolation

The JET hybrid scenario achieves high fusion performance by keeping plasma density low enough to decouple the ion and electron channel, and to allow NBI penetration right to the core. Assuming a fixed pedestal Greenwald density fraction, the best performance of the hybrid scenario is not at the maximum plasma current achievable in JET, and it remains an open question which plasma current will give the best fusion performance in DT conditions. In addition, future scenario development plans to increase the toroidal field from 2.8 T to 3.4 T (suitable steps for axial ICRH resonances at available frequencies) concomitant with the increase to maximum power, to keep β in the same domain. In this section, we use the predictive modelling capability developed in this work to guide the scenario development to the optimum plasma current and field. Simultaneously, our simulations integrate the

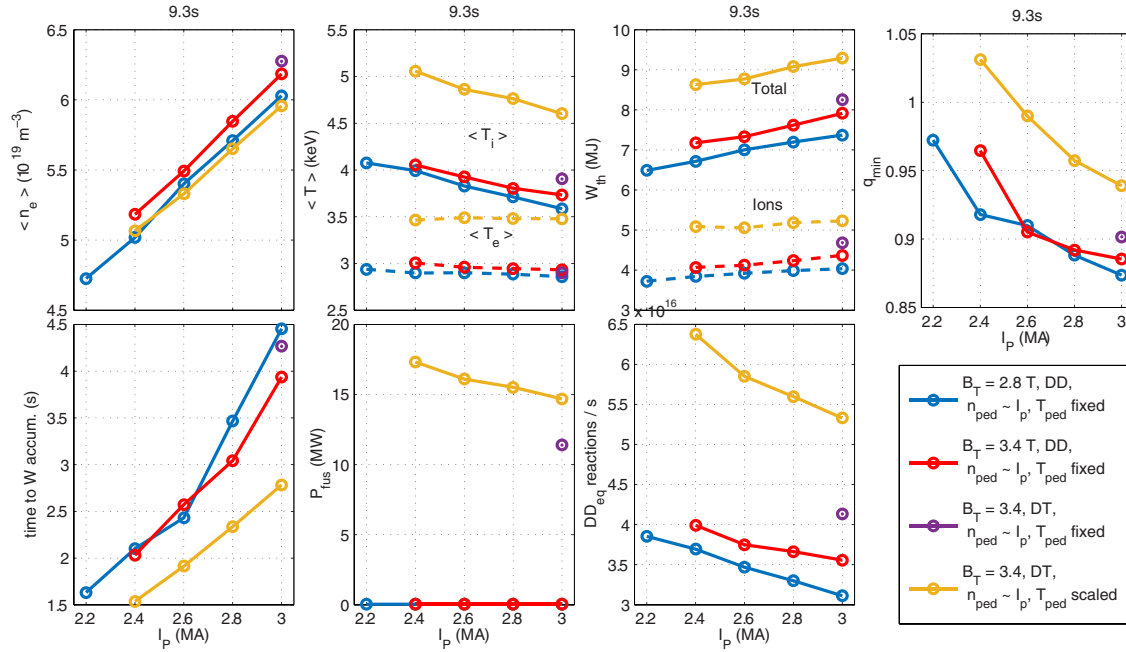


Figure 11. Global plasma confinement, fusion performance, current diffusion, and W accumulation predictions for current scans in DD and DT extrapolation, with fixed and extrapolated pedestals. The time to W accumulation is the from the start of the main heating phase until the core radiation from W first exceeds 0.15 MW, before any radiative collapse.

competing priorities of high performance and resistance to W accumulation.

We start from the simulation of 92398 (2.4 MA, 2.8 T) extrapolated to high power 32 MW NBI + 8 MW ICRH (axial, 80% on ions) in the previous section, most resistant to W accumulation. In the previous section, the pedestal was fixed to 92398 values, but in this section we extrapolate the pedestal based on a regression of the new JET-ILW pedestal database [63]. We extrapolate the pedestal-top density and pressure in input power and plasma current only (the data on the isotope scaling is sparse and the scaling is weak and uncertain) as follows

$$\begin{aligned} n_{e,extrap} &= n_{e,92398} \left(\frac{P_{extrap}}{P_{92398}} \right)^{-0.28} \left(\frac{I_{p,extrap}}{I_{p,92398}} \right)^{1.06} \\ p_{e,extrap} &= p_{e,92398} \left(\frac{P_{extrap}}{P_{92398}} \right)^{0.30} \left(\frac{I_{p,extrap}}{I_{p,92398}} \right)^{1.25} \end{aligned} \quad (2)$$

The ratio $T_{i,ped}/T_{e,ped} = 1.1$ at the pedestal top and the initial impurity concentrations (relative to n_e) are kept fixed as the pedestal is scaled. When scaling the plasma current, the initial q-profile for the simulations has been adapted to scale q_{95} appropriately, while keeping $q_0 = 1.2$ unchanged (in experiment, this is achieved by re-timing the start of the heating phase relative to the ramp-up). The different exponents between the pressure and density scaling mean there is a small but significant increase in temperature as both power and current are increased. The pedestal dependence on toroidal field is not modelled (as B cannot be differentiated from plasma current in the database).

The global OD properties, including fusion performance, current diffusion, and W accumulation, of current scans in both DD and DT are summarised in figure 11. The planned

increase in toroidal field from 2.8 T to 3.4 T at fixed q_{95} brings the expected benefit in fusion performance (up to 15%), and adding the scaling of the pedestal increases fusion performance up to 28%. The predictions also show that in all cases the fusion performance decreases with current (and density), as ion-electron coupling increases and beam penetration decreases; with this pedestal scaling, the increase of temperature with current is not strong enough to overcome the increase in ion-electron coupling. This is consistent with previous work [64] which used a stronger pedestal scaling with current (based on JET-C) [65]. It is worth noting that the isotope scaling and predicted fusion power are similar to those presented for the JET hybrid in [64], albeit with a different mechanism for the isotope scaling (in that work ETG scales were not included and the isotope enhancement from ExB shear played the dominant role, using a different transport model).

The resistance of the scenario to W accumulation is indicated in figure 11 by the time at which radiation in the volume $\rho < 0.2$ first exceeds 0.15 MW (t_{accum}). Practically speaking, this low level of core radiation does not pose a problem for the simulation or the experiment, but is convenient to compare the various simulations, since *all* simulations exceed this value at some point in their evolution. In a subset of simulations, a later radiative axial temperature collapse begins around the time the radiation within $\rho > 0.2$ exceeds 1 MW ($t_{collapse} \sim 2t_{accum}$), beyond which the simulation becomes numerically unstable (in these conditions in an experiment, a disruption is likely). The increase in plasma density with current brings a significant benefit of reduced density peaking (figure 13) and delayed W accumulation (figure 12); an increase in the pedestal top density by 18% between 2.4 MA and 2.8 MA brings a 1 s delay

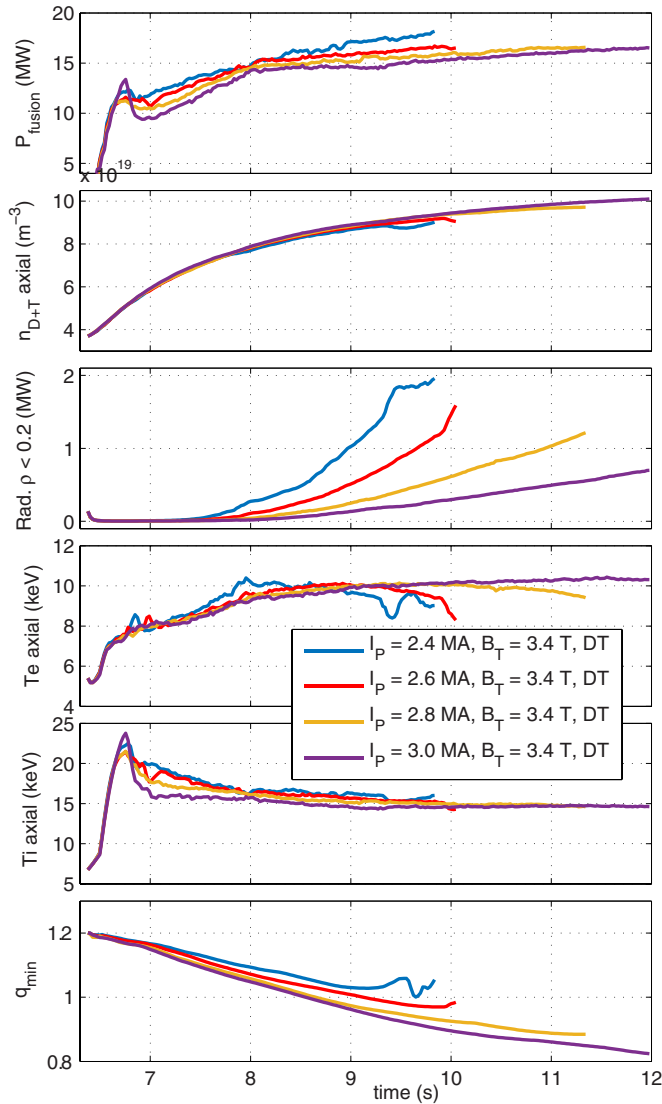


Figure 12. Predicted scenario evolution of DT extrapolated cases. All cases have been extrapolated from 92398 in toroidal field, heating power, pedestal and isotope, for the presented current scan. Each trace ends when the simulation becomes numerically unstable due to axial radiative collapse.

in the start of W accumulation, and a 2 s delay in the radiative collapse, at the cost of a 11% loss in fusion performance. We have also demonstrated that increasing the plasma density independently of the plasma current (e.g. by increased triangularity) brings a similar delay in W accumulation [66].

However, in the higher current pulses, current diffusion gives $q_{\min} < 1$ well before any significant W accumulation. The present simulations (with no MHD model) continue to predict increasing density, stored energy and fusion performance after $q_{\min} < 1$. This evolution is determined by the resistive timescale, in experiment the actual performance would be limited by MHD unless the q profile can be further optimised. At $P_{\text{in}} = 40$ MW, $B_T = 3.4$ T, $I_p = 3.0$ MA, q_0 remains above 1 at least 2 s into the heating phase, but a fully integrated solution for a 5 s scenario will likely require a re-tailoring the q -profile during ramp-up (for an initial $q_0 < 1.2$), or a

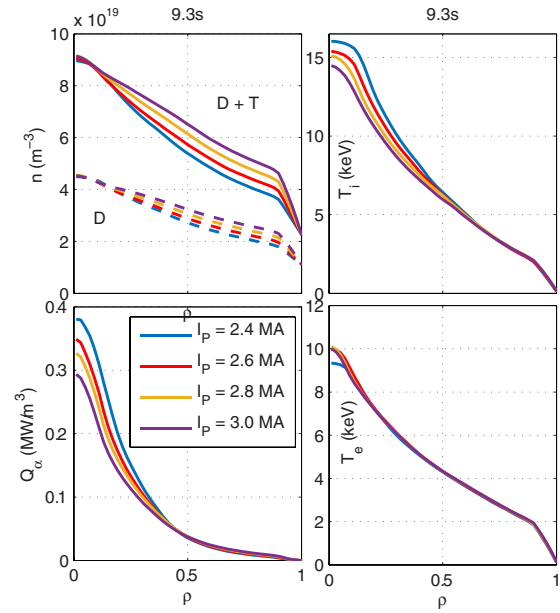


Figure 13. Bulk profiles and alpha-heating power for DT extrapolated cases from (figure 12), at $t_{\text{NBI}} + 3$ s = 9.3 s.

strategy which tolerates 1,1 MHD but avoids triggering tearing modes; this remains a challenge to optimise in the scenario development.

Each of the points in figure 11 represents a complex evolving multi-channel simulation; as example, we present the evolution and profiles of the DT case with pedestal extrapolation in figures 12 and 13. (The complete outputs of all cases are available for JET collaborators to analyse and use, as listed in appendix 4). The scenario initially undergoes a hot ion transient of extreme ion-electron decoupling, but this phase is not the highest fusion power in the evolution: As the density rises, the ion temperature falls, but the fusion power does not saturate until more than 2 s after the establishment of H-mode. The current continues to slowly diffuse throughout the full period of all simulations. The density and W peaking never entirely saturate in any case, but the simulations indicate that the case at 3.0 MA (with 32 MW NBI and 8 MW of axial ICRH heating 80% to the ions) is sufficiently resilient to W accumulation to survive the full 5 s.

Overall, these simulations suggest the hybrid scenario may be able to avoid axial W accumulation for up to 5 s if it operates at 2.8 MA or greater, but that higher transient performance can be achieved at lower currents and densities. In lower density conditions, axial accumulation is inevitable in a 5 s H-mode, and the scenario must be able to tolerate hollow electron temperature profiles or rely on benign (1,1) MHD to keep the W concentration under control while also avoiding neoclassical tearing modes.

7. Summary and discussion

This work demonstrates the integration of multiple first-principle based models into a powerful multi-channel predictive tool for the core plasma, which can reproduce

observed W accumulation and ICRH mitigation in JET, and is able to guide JET scenario development to optimise future plasmas. The modelling capability is applied to investigate the optimal ICRH scheme to resist W accumulation in the hybrid scenario, scanning power density and ion-electron heating fraction, to help JET reach its objective of high performance in steady conditions (5 s). High power density located near the axis, is predicted to be most effective in delaying the central W accumulation, in agreement with experimental findings. In JET hybrid conditions (strong rotation and T_i decoupled from T_e) where neoclassical convection dominates W transport, our simulations predict that ion heating schemes (e.g. He-3 minority, or 3-ion schemes) increase neoclassical temperature screening and could be more efficient for central W control. In scenarios where ions and electrons are coupled, or in lower rotation devices such as ITER (where turbulent W transport dominates), electron heating is expected to be more effective for core W control. The modelled system contains multiple non-linearities, and the W accumulation phase is extremely sensitive to heating power density.

Supporting high-fidelity ICRH modelling (including the effects of finite orbit widths) finds that these requirements can be met by axial He-3 minority heating, which will deliver both higher power density and greater ion heating compared to H minority schemes. Finite orbit width effects have an important impact on ICRH, as they spread the power deposition and reduce the impact of fast ions on neoclassical temperature screening. Further cross-code validation effort is needed to improve confidence in ICRH modelling with orbit width effects and with a closed coupling between the full wave field and distribution function. The effect of ICRH fast ion anisotropy on W asymmetry and neoclassical transport has been parametrised with a fast ion distribution which accounts for the lower asymmetry resulting from high field resonances. The anisotropy impact on W transport is found to be negligible compared to the poloidal asymmetry generated by the high rotation of the JET highest power hybrid discharges. At lower rotations (such as in the JET baseline scenario), a resonance about 10 cm on the low field side is found to be optimal for reducing W poloidal asymmetry and neoclassical transport.

The modelling capability has also been used to predict scenario and W evolution in planned TT and DT hybrid plasmas, and predicts improved core confinement with heavier isotope, due to decreased ion-electron coupling, increased T_i/T_e and stabilisation of the ITG mode. Extrapolations to planned full power (40 MW) DT plasmas predict 14.8 MW of fusion power with conservative pedestal assumptions, and up to 17.5 MW using the JET-ILW pedestal database scaling. Unfortunately, the positive scaling of core confinement with isotope comes with greater density peaking and a tendency for earlier W accumulation, which will make achievement of a stationary high performance hybrid scenario a challenge. Increasing the pedestal density (either through increased plasma current, or its expected isotopic dependence) presents one solution; less central beam deposition delays density peaking and W accumulation, at some cost in fusion power. This

mitigation of increased pedestal density and reduced density peaking is relevant for core W control also in the baseline scenario. Future modelling and experiments will seek an optimisation between plasma current, pedestal density, q profile evolution and performance to build a stationary high performance hybrid plasma. It remains to be demonstrated if stationarity can be achieved in MHD-free conditions, or if benign 1,1 MHD activity can be tolerated, or exploited to prevent axial W build-up.

The predictions made here for isotope scaling and W accumulation are specific to plasmas with $T_i > T_e$, and depend on the inclusion of ETG transport within a quasilinear transport model, which remains to be verified by non-linear multi-scale gyrokinetics in these conditions. These predictions are made in advance of planned experiments and will be tested as JET operates with higher power and tritium isotope in the coming campaigns.

Acknowledgments

This work has been carried out within the framework of the EUROfusion Consortium and has received funding from the Euratom research and training programme 2014–2018 and 2019–2020 under Grant Agreement No. 633053. The views and opinions expressed herein do not necessarily reflect those of the European Commission. The work was also supported in part by the Swiss National Science Foundation. The Piz Daint (CSCS, Switzerland) and the MARCONI-Fusion (CINECA/ENEA, Italy) supercomputer facilities were used for the simulations presented in this research. Numerical calculations using Piz Daint were supported by a grant from CSCS under Projects s914 and s821. F.J. Casson appreciated helpful discussions with C. M. Roach, D. Van Eester, D. Gallart, and J. Garcia. F.J. Casson also wishes to thank all those who have contributed to the JINTRAC codes over many years, especially Adolfo Taroni, original author of JETTO, who sadly passed away while this work was in press.

Appendix 1: Validation of electromagnetic stabilisation correction for QuaLiKiz transport model

In fully predictive multi-channel simulation, a poor prediction in one bulk channel can influence the turbulence dynamics and impurity transport, and degrade the ability of the simulation to predict the overall evolution of the scenario. To achieve the accurate multichannel predictive capability presented in this work, it was necessary to correct the results of the electrostatic QuaLiKiz model to mimic the effect of electromagnetic (EM) stabilisation of the ITG instability, known to be significant in JET hybrid [16].

An ad-hoc EM correction model was developed, in which the ∇T_i inputs to QuaLiKiz are reduced by a factor of the local $\beta_{\text{thermal}}/\beta_{\text{total}}$, (between 0.7 and 1 in the discharges presented) shifting the ITG threshold, and correcting the under-prediction

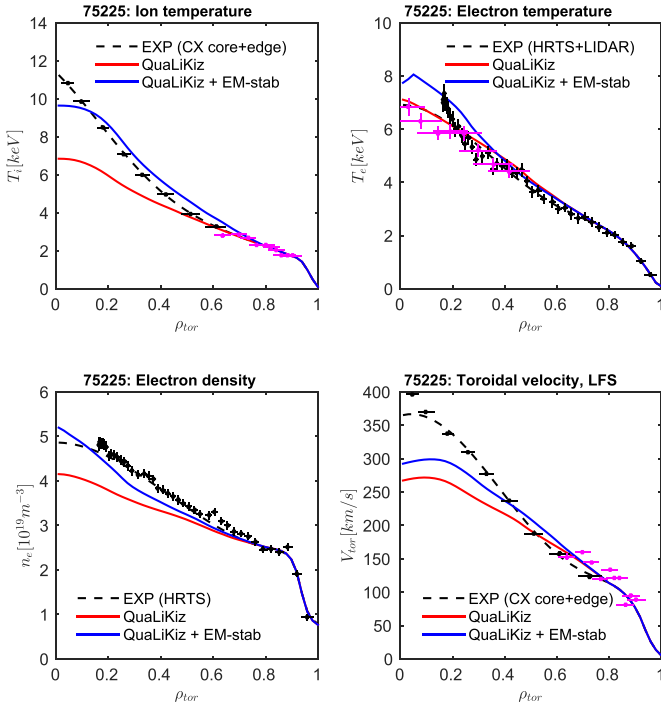


Figure A1. Validation of electromagnetic stabilisation correction for QuaLiKiz on JET-C hybrid discharge 75225 (6.0–6.5 s).

of T_i otherwise observed in QuaLiKiz simulations of hybrid discharges [5, 13]. The factor used emphasises ITG nonlinear EM-stabilisation effects, enhanced by fast ions, cross-correlated in JET with total β and EM stabilisation [16–20].

The JET discharge 75225 (NBI 18 MW, $I_p = 1.6$ MA, $B_T = 1.9$ T), known to demonstrate significant electromagnetic turbulence stabilisation [16], was used for validation of the EM correction model. This discharge has similar temperatures and densities to the JET-ILW pulse 92398 studied in most of this paper, albeit at lower power, field, current, and rotation. Temperature, density and rotation were all predicted self consistently using the same settings as for 92398, but without the presence of heavy impurities and with the faster NCLASS transport model.

The results of the validation, presented in figure A1 show that the EM correction factor acts primarily to increase the ion temperature and density predictions in the core, giving a much closer agreement with experiment while not significantly impacting the rotation or electron temperature predictions. Significantly for this work, the density peaking in the core, which drives W accumulation, is predicted correctly only with the EM stabilisation. The level of agreement in each channel is quantified in table A1, using the RMS relative error (as used in [13]). The validation metric shows that all profiles are predicted within 12% error if the EM stabilisation model is included, but error rises to 24% in the ion temperature channel and 19% in the momentum channel if it is not included. This model has also been validated successfully in high-power JET baseline discharges [67].

Table A1. RMS relative error between the predicted and experimental fitted profiles. The RMS error is averaged uniformly over the profile between $0.1 < \rho < 0.8$. This metric weights accuracy in central predictions, important for this paper, more strongly than volume averaged quantities.

Model	T_i	T_e	n_e	v_{tor}
QuaLiKiz	0.241	0.050	0.132	0.188
QuaLiKiz + EM-stab	0.078	0.108	0.054	0.120

Appendix 2: Interface between NEO and JETTO

To enable this work, a new interface was developed between the JETTO transport solver and the NEO transport model; this interface necessarily includes poloidal asymmetries. Since JETTO solves 1.5D transport equations, the transported quantities described by its equations must be flux functions. For a poloidally asymmetric impurity such as W, the transport equations must describe the flux surface averaged (FSA) value of the density (this is the most natural choice to ensure particle conservation) [2]. NEO uses the low field side (LFS) densities as input, and computes the 2D distribution internally, because the transformation $n_{\text{LFS}}(\rho) \rightarrow n(\rho, \theta) \rightarrow n_{\text{FSA}}(\rho)$ is convenient to compute (the potential $\Phi(\rho, \theta)$ must be found numerically from the quasi-neutrality constraint [68], for a general number of species; NEO uses the Newton-Raphson method). In order to couple JETTO to NEO it is necessary to compute the inverse transformation $n_{\text{FSA}}(\rho) \rightarrow n_{\text{LFS}}(\rho)$. To achieve this in the JETTO–NEO interface, we implemented another 2D poloidal asymmetry numerical solver computing $n_{\text{LFS}}(\rho) \rightarrow n_{\text{FSA}}(\rho)$, (generalised from the root finding method described in [68]), and built a second layer which iterates to find the $n_{\text{LFS}}(\rho)$ required for the $n_{\text{FSA}}(\rho)$ given by JETTO. The advantage of computing the 2D $n(\rho, \theta)$ in the interface (duplicating a computation available in NEO) is that it can be reused to add centrifugal transport corrections outside a transport model [69] or to build the reduced neoclassical model described in [45]. The poloidal asymmetry solver in the JETTO–NEO interface has been verified against the poloidal asymmetries computed by GKW and NEO [68, 70] and QuaLiKiz [13]. While JETTO and standalone NEO both have a full geometry description, the JETTO–NEO interface assumes up-down symmetric geometry (since only three moments are presently passed to the interface).

The remainder of the JETTO–NEO interface has been verified by comparing the ion heat transport with NCLASS, and by comparing the predicted steady state W profile predicted by JETTO–NEO (with bulk channels interpretive) to the profile predicted with standalone NEO (figure A2). The difference between full geometry in the standalone NEO run and the 3-moment description in JETTO–NEO is the likely cause of the deviation at the outer radii. The n_{LFS} profile is predicted from standalone NEO by finding the zero flux density gradient for several radii, and integrating across the profile (the method used in [2, 3, 6, 33]). A trace level of W was used, and anomalous turbulent diffusion was added using the Bohm–GyroBohm model [27] at 3% of the standard values

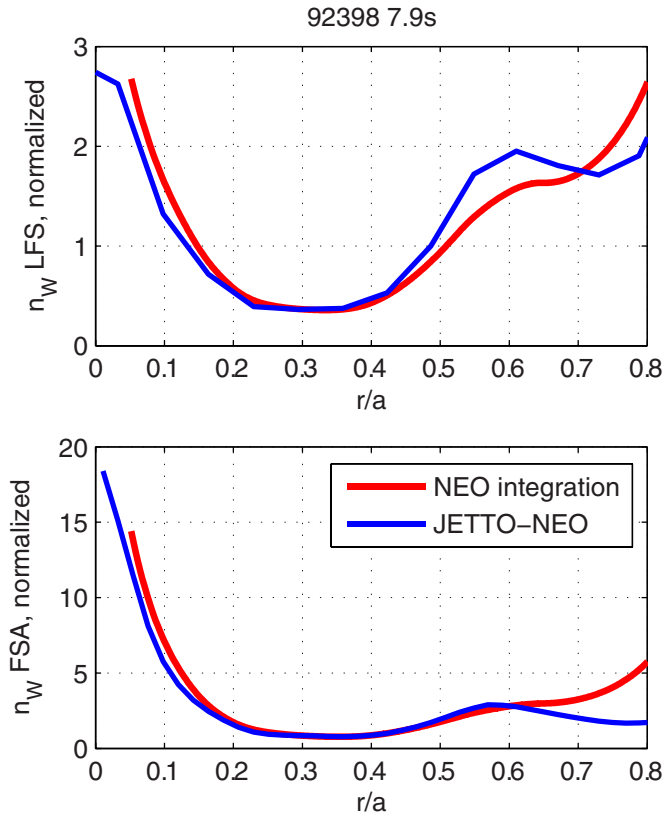


Figure A2. Verification of the JETTO–NEO interface including strong rotation: The predicted steady state W profile from JETTO–NEO is compared with the integration of the peaking factor (zero-flux density gradient) predicted by standalone NEO. Since the latter cannot provide absolute W densities, the n_{FSA} profiles are normalised to the mid radius value.

(in the trace limit, neoclassical W diffusion is negligible). In both cases, only the average local charge state of W is simulated in NEO. JETTO retains the ionisation and recombination of all charge states, which allows for non-coronal charge state distributions (more significant in the outer plasma). The standalone NEO integration method transforms the *output* transport coefficients from LFS values to FSA values (using the transformations defined in [2]) which can then be integrated to find $n_{\text{FSA}}(\rho)$. This method is entirely different to the method of $n_{\text{FSA}}(\rho) \rightarrow n_{\text{LFS}}(\rho)$ *input* transformation described above for the JETTO–NEO interface; the fact that both sets of n_{FSA} and n_{LFS} profiles agree in figure A2 serves as an additional verification of the validity of both approaches.

In the JETTO–NEO interface, NEO (which is a local model) is parallelised over the radial grid points. The computational time taken by NEO scales factorially with the number of species, due to the number of interactions that must be evaluated in the full collision operator. In the multispecies simulations presented in this work, NEO is the bottleneck of the simulated system and must be run at limited resolution to enable tractable simulations (the longest of our simulations take 3 weeks on 16 cores (Intel Xeon E5-2665)). For all multichannel simulations, NEO uses 16 radial points, 17 poloidal

points, 5 energy grid polynomials and 13 pitch angle polynomials (which is sufficient to resolve the collisional regime of W), and the transport coefficients are updated at most every 1×10^{-4} s (which is sufficient to resolve the fastest neoclassical transport timescales). In all JETTO–NEO simulations, a physically negligible (but non-zero) source of W is injected from the SOL; this avoids regions of zero W density near the last closed flux surface (since the pedestal has a strong inward convention) which are numerically unstable for the transport solver.

The diffusive and convective parts of the neoclassical flux are not split in any of the JETTO–NEO simulations in this work, since this doubles the number of evaluations of NEO required and adds numerical complexity (this option is implemented in the interface, but not used here). A faster neoclassical transport model including the effects of poloidal asymmetry (such as [45]) would benefit future predictive simulations of W transport, if sufficient accuracy can be achieved.

Appendix 3: Mapping between two descriptions for anisotropic fast ions in SCENIC–NEO Interface

In the following discussion, poloidal asymmetries generated by anisotropy are discussed. An anisotropic minority acts indirectly on neoclassical W transport, through its contribution to the parallel force balance leading to a poloidal electric field which modifies the W asymmetry [71]. For brevity, we present here only the low rotation limit, i.e. in the absence of the centrifugal inertial force. The anisotropic and inertial mechanisms generating poloidal asymmetries are independent (both are included in NEO and the JETTO interface), and are combined in our numerical solution as independent factors in the form for the poloidal density variation.

Following the presentation and notation of [8], the distribution of the supra-thermal anisotropic minority can be accurately parametrised with the Dendy [72] distribution

$$f_{\text{fast}}(\mu, \mathcal{E}, r) = \left(\frac{m}{2\pi}\right)^{3/2} \frac{n_{\text{ic}}(r)}{T_{\perp, \text{ic}} T_{\parallel, \text{ic}}^{1/2}} \exp\left\{-\frac{\mu B_{\text{ic}}}{T_{\perp, \text{ic}}} - \frac{|\mathcal{E} - \mu B_{\text{ic}}|}{T_{\parallel, \text{ic}}}\right\} \quad (\text{A3.1})$$

where $\mu = mv^2/2B$ is the magnetic moment, \mathcal{E} is the particle energy, r is the magnetic surface label, and the subscript ‘ic’ stands for a quantity evaluated at the IC resonance points on the surface labelled by r .

As shown first in [73], the density moment of the fast distribution A3.1 integrates to

$$n(r, \mathcal{B}; \mathcal{T}) = n_{\text{ic}}(r; \mathcal{T}) N(r, \mathcal{B}; \mathcal{T}) \quad (\text{A3.2})$$

with the density form factor

$$N(r, \mathcal{B}; \mathcal{T}) = \mathcal{T}_- \left[1 + \left(\frac{\mathcal{T}_+}{\mathcal{T}_-} - 1\right) \sqrt{\frac{\mathcal{T}_-}{\mathcal{B}} (\mathcal{B} - 1)} H(\mathcal{B} - 1)\right] \quad (\text{A3.3})$$

where $\mathcal{T}_{\pm} = [\mathcal{B} \pm (\mathcal{B} - 1) \mathcal{T}]^{-1}$ with $\mathcal{T} = T_{\perp, \text{ic}}/T_{\parallel, \text{ic}}$ and $\mathcal{B} = B_{\text{ic}}/B$, and where H is the Heaviside function. The notations and expressions in [8] and [73] have different presentations, but we have verified that they are the same. In the Dendy parametrisation, neither T_{\parallel} or T_{\perp} are flux functions. As demonstrated in [8], the density moment A3.2 differs significantly

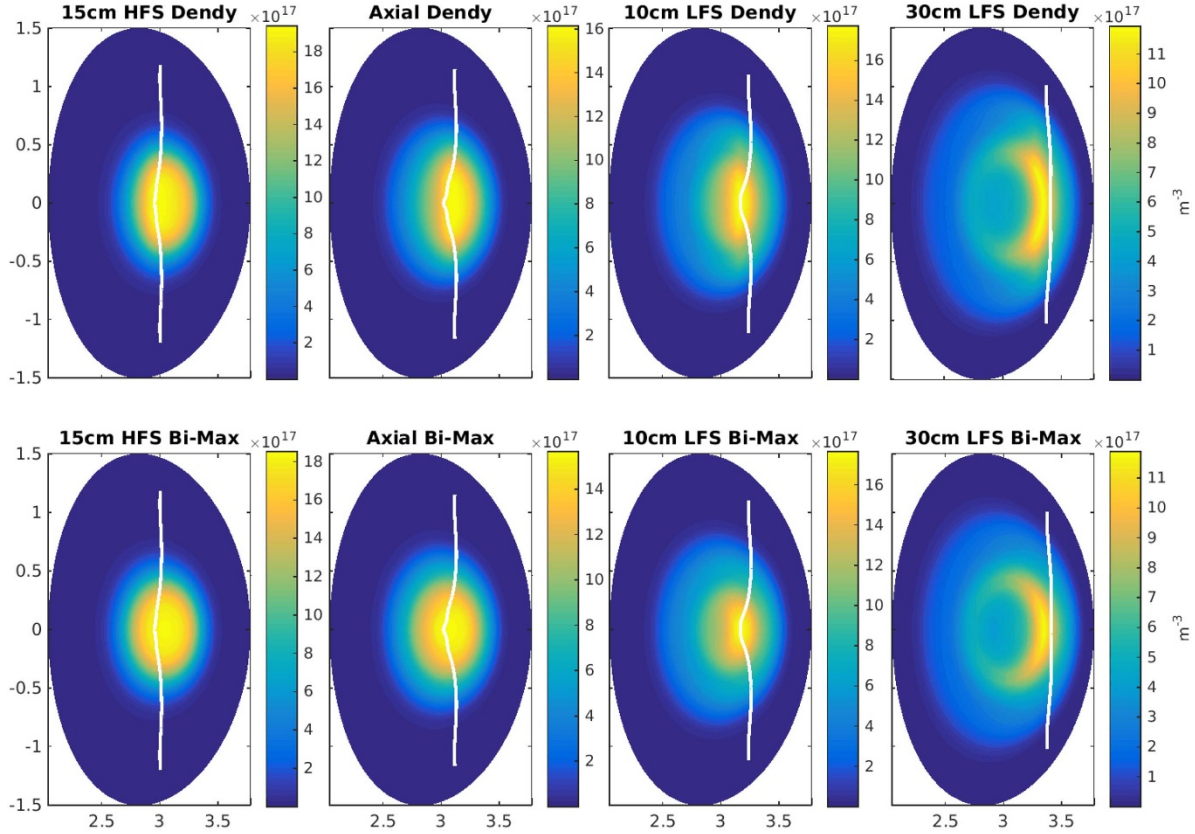


Figure A3.1. Density of anisotropic supra-thermal H minority in SCENIC resonance scan with 4.5 MW ICRH coupled to the plasma. The background profiles including rotation and ionization state are taken from 92398 at 7.9 s, global H concentration is 2.5%. The top row uses the Dendy parametrization for the fast ions (equation A3.1). The bottom row uses a Bi-Maxwellian model (equation A3.5) with additional geometric factors (equation A3.6). The plots are produced from the (up-down symmetric) JETTO–NEO transport code interface, which calculates the 2D distributions for all ions, and converts the inputs into the Bi-Maxwellian description for use in NEO. The resonance location is indicated by the white line.

for high field side (HFS) and low field side (LFS) resonances, with LFS resonances leading to much larger poloidal asymmetries.

The anisotropic minority distribution may also be less accurately parametrised by a Bi-Maxwellian

$$f_{fast}(v_{\perp}, v_{\parallel}) = \left(\frac{m}{2\pi}\right)^{3/2} \frac{n}{T_{\perp} T_{\parallel}^{1/2}} \exp\left\{-\frac{mv_{\parallel}^2}{2T_{\parallel}} - \frac{mv_{\perp}^2}{2T_{\perp}}\right\} \quad (\text{A3.4})$$

which integrates over velocity space to give the density

$$n(\theta) = n_{R0} \left[\frac{T_{\perp, R0}}{T_{\parallel}} + \left(1 - \frac{T_{\perp, R0}}{T_{\parallel}}\right) \frac{B_{R0}}{B(\theta)} \right]^{-1} \quad (\text{A3.5})$$

where T_{\parallel} is a flux function, but T_{\perp} is not, and $R0$ denotes a major radius for each flux surface at which functions of the poloidal angle θ are evaluated to define a constant of integration. In what follows, $R0$ is always evaluated at the LFS, consistent with the input definitions used in NEO.

The Bi-Maxwellian parametrization permits the simplest description of anisotropy, but cannot capture details in the velocity space resolution around the IC resonance points [8]. For LFS resonances, tangent to the flux surface with $R_{ic} = R_{LFS} = R0$, the two descriptions are equivalent. In previous work [6, 33], the form factor A3.5 was used also to describe

all other resonances, with $T_{R0} = T_{LFS}$ taken as the flux surface average of energy moment from TORIC simulations. This approximation results in identical asymmetries for both LFS and HFS resonances, and a strong overestimate of the asymmetry generated by HFS resonances.

The Bi-Maxwellian description (A3.4, A3.5) is the form implemented for anisotropic species in NEO, since it is a practical form to enter in the collision operator, which is built on Legendre polynomials in velocity space [11]. Describing arbitrary fast ion distributions efficiently and accurately in NEO could require the development of a different numerical scheme, beyond the scope of the present work: Here we assume that a correct description of the neoclassical W transport is not sensitive to the details of the minority distribution, as long as the asymmetry of the W is correctly described.

In order to couple the results of the high-fidelity SCENIC modelling to NEO, we prescribe a new mapping between the density form factors A3.3 and A3.5, to capture the dependence on resonance location (missing in previous work [6, 33]) via a geometric approximation. The SCENIC supra-thermal minority distribution is parametrised by equation (A3.1) and the parameters $\mathcal{T}, n_{ic}, T_{\text{eff}}$, where T_{eff} is the equivalent temperature of the flux surface averaged energy moment. These are mapped to the Bi-Maxwellian asymmetry (A3.5) as

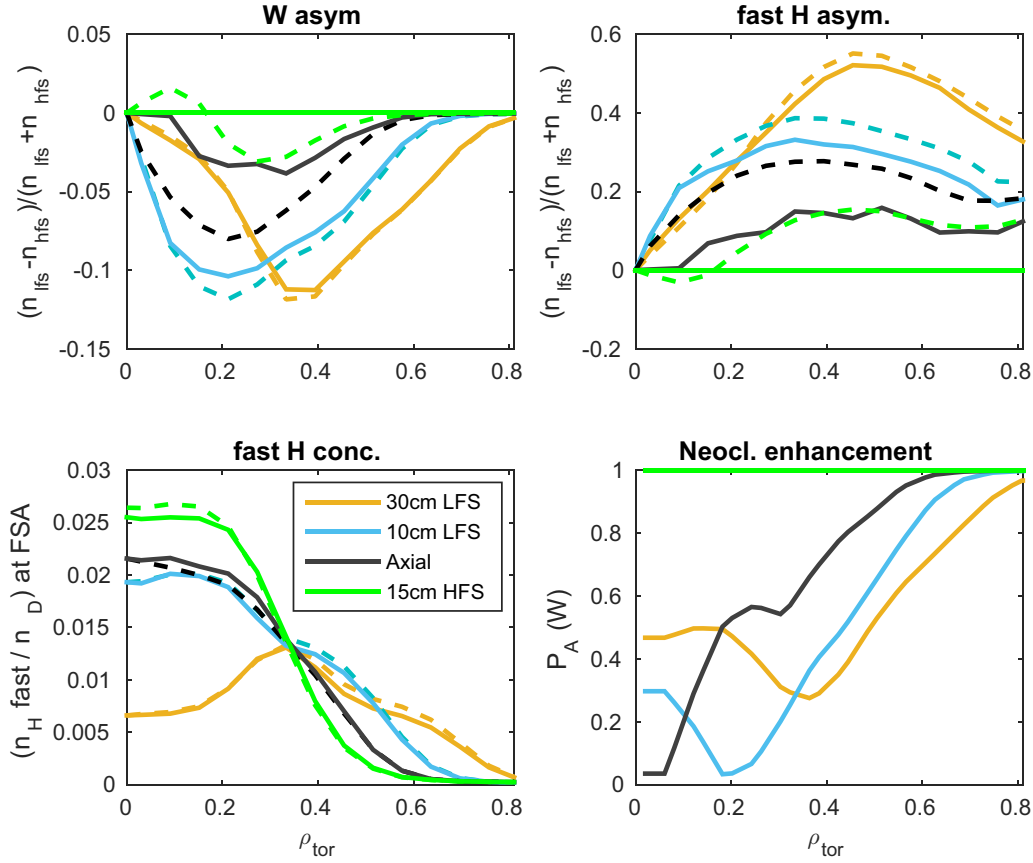


Figure A3.2. Asymmetry factors for W and supra-thermal H minority compared for the Dendy (dashed) and geometrically adapted Bi-Maxwellian (solid) parametrisations for the resonance scan in figure A3.1. The enhancement factor for neoclassical W transport due to poloidal asymmetry is computed, only for the bi-Maxwellian description (which is interfaced to NEO).

$$\begin{aligned}
 n_{LFS} &= n_{ic} N_{LFS}, \\
 T_{\perp} &= T_{\parallel} = T_{\text{eff}} \text{ (isotropic)} \quad \text{for } R_{\text{geo}} < R_{\text{ic}} \\
 &\quad \text{(HFS resonance)} \\
 T_{\perp, LFS} &= \frac{3T_{\text{eff}}}{2+T}, \quad T_{\parallel} = \frac{3T_{\text{eff}}}{1+2T} \quad \text{for } R_{\text{ic}} < R_{\text{geo}} < R_{\text{ic}} - r_{\text{minor}} \\
 &\quad \text{(LFS resonance)} \\
 \hat{T} &= T \sqrt{\cos(\theta_{\text{ic}})}
 \end{aligned} \tag{A3.6}$$

where R_{geo} is the geometric centre of the flux surface and θ_{ic} is the poloidal angle at which the resonance intersects the flux surface (up-down symmetry assumed). This mapping preserves the total energy (effective temperature) of the minority, and neglects the smaller impact of high field side resonances on the poloidal asymmetry. For resonances which intersect the flux surface between R_{geo} and R_{LFS} , the cosine function gives a smooth transition up to the maximum anisotropy and asymmetry when $R_{\text{ic}} = R_{\text{LFS}}$.

The geometrically-adapted Bi-Maxwellian description (A3.6) is compared to the more accurate Dendy description for a SCENIC resonance scan shown in figures A3.1 and A3.2. The geometric approximation captures well the asymmetry for low field side resonances and slightly underestimates the pressure anisotropy and asymmetry for axial and HFS resonances.

It gives an upper bound to the difference between HFS and LFS resonances, and provides an effective interface to discriminate between them in NEO calculations.

In the resonance scan, the LFS resonances closer to the axis produce larger supra-thermal concentrations, but lower H asymmetries, compared to less central LFS resonances (figure A3.1). These two trends counteract when combined in the anisotropic pressure, so that the W asymmetry is not particularly sensitive to resonance location (as long as it is on the LFS). We also note that the W asymmetry factors generated are much smaller than those due to rotation (figure 3(a)) under JET high power conditions (dominant NBI heating).

Appendix 4: Source code and simulation data

The simulations presented above are archived in the JET processed pulse file (PPF) system and JETTO simulation catalogue, and are available for all JET collaborators to analyse in more detail. All JETTO data are stored under pulse 92398 in private PPF under user ID fcasson.

Source code versions used for presented integrated simulations:

Code Name	git repository	git commit ID	git tag
JETTO	ssh://git@git.iter.org/scen/jetto.git	b810c907ee5ad19 c	fcasson_v080817_NF_2020
NEO	https://github.com/gafusion/gacode	63244a30f013d7e1	—
QualiKiz	https://gitlab.com/qualikiz-group/QualiKiz.git (http://www.qualikiz.com/)	7efc8659bdfaf2119	JETTO-Release-v080817

Fully predictive multi-channel simulations:

Description	JETTO ID	PPF					
		seq. no	Current	Field	Pedestal	Heating	Isotope
92398 8-channel validation, PION on axis	fcasson/jetto/jet/92398/dec1318/seq#1	3139	2.2 MA	2.8 T	92398	26 + 4ei	DD
RF power scan, 8 MW 50:50 e-i	fcasson/jetto/jet/92398/dec1818/seq#7	3164	2.2 MA	2.8 T	92398	32 + 8ei	DD
RF power scan, 4 MW 50:50 e-i	fcasson/jetto/jet/92398/dec2018/seq#4	3156	2.2 MA	2.8 T	92398	32 + 4ei	DD
RF power scan, 0 MW 50:50 e-i	fcasson/jetto/jet/92398/dec2018/seq#5	3158	2.2 MA	2.8 T	92398	32 + 0ei	DD
RF width scan, wide on axis 50:50 e-i	fcasson/jetto/jet/92398/feb1219/seq#2	3249	2.2 MA	2.8 T	92398	32 + 8ei	DD
RF width scan, wide off axis 50:50 e-i	fcasson/jetto/jet/92398/dec2018/seq#3	3155	2.2 MA	2.8 T	92398	32 + 8ei	DD
RF width scan, narrow on axis 50:50 e-i	fcasson/jetto/jet/92398/dec1818/seq#7	3164	2.2 MA	2.8 T	92398	32 + 8ei	DD
RF e-i scan, 80% ions, narrow on axis	fcasson/jetto/jet/92398/feb1219/seq#1	3221	2.2 MA	2.8 T	92398	32 + 8i	DD
RF e-i scan, 80% elec, narrow on axis	fcasson/jetto/jet/92398/dec1818/seq#2	3152	2.2 MA	2.8 T	92398	32 + 8e	DD
RF e-i scan, 50:50, narrow on axis	fcasson/jetto/jet/92398/dec1818/seq#3	3153	2.2 MA	2.8 T	92398	32 + 8ei	DD
W content scan, 100% of 92398	fcasson/jetto/jet/92398/feb1219/seq#1	3221	2.2 MA	2.8 T	92398	32 + 8i	DD
W content scan, 50% of 92398	fcasson/jetto/jet/92398/dec1818/seq#9	3166	2.2 MA	2.8 T	92398	32 + 8i	DD
W content scan, 150% of 92398	fcasson/jetto/jet/92398/dec1818/seq#8	3165	2.2 MA	2.8 T	92398	32 + 8i	DD
Current scan 2.8 T, fixed pedestal	fcasson/jetto/jet/92398/nov2318/seq#2	3034	2.2 MA	2.8 T	92398	32 + 8i	DD
Current scan 2.8 T, fixed pedestal	fcasson/jetto/jet/92398/nov2318/seq#3	3035	2.4 MA	2.8 T	ne~Ip	32 + 8i	DD
Current scan 2.8 T, fixed pedestal	fcasson/jetto/jet/92398/nov2318/seq#6	3146	2.6 MA	2.8 T	ne~Ip	32 + 8i	DD
Current scan 2.8 T, fixed pedestal	fcasson/jetto/jet/92398/dec2018/seq#1	3147	2.8 MA	2.8 T	ne~Ip	32 + 8i	DD
Current scan 2.8 T, fixed pedestal	fcasson/jetto/jet/92398/nov2318/seq#4	3036	3.0 MA	2.8 T	ne~Ip	32 + 8i	DD
Current scan 3.4 T, fixed pedestal	fcasson/jetto/jet/92398/nov2418/seq#1	3030	2.4 MA	3.4 T	ne~Ip	32 + 8i	DD
Current scan 3.4 T, fixed pedestal	fcasson/jetto/jet/92398/nov2418/seq#2	3031	2.6 MA	3.4 T	ne~Ip	32 + 8i	DD
Current scan 3.4 T, fixed pedestal	fcasson/jetto/jet/92398/nov2418/seq#3	3032	2.8 MA	3.4 T	ne~Ip	32 + 8i	DD
Current scan 3.4 T, fixed pedestal	fcasson/jetto/jet/92398/nov2318/seq#1	3033	3.0 MA	3.4 T	ne~Ip	32 + 8i	DD
Isotope scan at 3.4 T, 3.0 MA	fcasson/jetto/jet/92398/dec1818/seq#4	3160	3.0 MA	3.4 T	ne~Ip	32 + 8i	DT
Isotope scan	fcasson/jetto/jet/92398/feb1219/seq#1	3221	2.2 MA	2.8 T	92398	32 + 8i	DD
Isotope scan	fcasson/jetto/jet/92398/nov2418/seq#6	3150	2.2 MA	2.8 T	92398	32 + 8i	TT
Isotope scan, with alpha heating	fcasson/jetto/jet/92398/nov2418/seq#5	3148	2.2 MA	2.8 T	92398	32 + 8i	DT
Isotope scan, no alpha heating	fcasson/jetto/jet/92398/dec1818/seq#10	3167	2.2 MA	2.8 T	92398	32 + 8i	DT
Isotope scan, no ETG	fcasson/jetto/jet/92398/nov2418/seq#4	3038	2.2 MA	2.8 T	92398	32 + 8i	DT
Isotope scan, no ETG	fcasson/jetto/jet/92398/nov2518/seq#1	3039	2.2 MA	2.8 T	92398	32 + 8i	DD
Isotope scan, no ExB	fcasson/jetto/jet/92398/nov2518/seq#2	3040	2.2 MA	2.8 T	92398	32 + 8i	DD
Isotope scan, no ExB	fcasson/jetto/jet/92398/nov2618/seq#1	3151	2.2 MA	2.8 T	92398	32 + 8i	DT
DT current scan 3.4 T, pedestal scaled	fcasson/jetto/jet/92398/mar1319/seq#2	3458	2.4 MA	3.4 T	scaled	32 + 8i	DT
DT current scan 3.4 T, pedestal scaled	fcasson/jetto/jet/92398/mar1419/seq#1	3462	2.6 MA	3.4 T	scaled	32 + 8i	DT
DT current scan 3.4 T, pedestal scaled	fcasson/jetto/jet/92398/jun2419/seq#1	3490	2.8 MA	3.4 T	scaled	32 + 8i	DT
DT current scan 3.4 T, pedestal scaled	fcasson/jetto/jet/92398/jun2519/seq#2	3487	3.0 MA	3.4 T	scaled	32 + 8i	DT

W-only predictive simulations (interpretive bulk plasma) to isolate impact of ICRH anisotropy on neoclassical transport (as shown in section 4):

Description	IC resonance	JETTO ID	PPF seq. no.	Heating	Rotation
92398 rotation, No ICRH anisotropy	None	fcasson/jetto/jet/92398/mar1819/seq#14	3432	N/A	High
92398 rotation, SCENIC IC res scan	30 cm LFS	fcasson/jetto/jet/92398/mar1819/seq#5	3423	4.5 MW IC	High
92398 rotation, SCENIC IC res scan	10 cm LFS	fcasson/jetto/jet/92398/mar1819/seq#4	3422	4.5 MW IC	High
92398 rotation, SCENIC IC res scan	Axial	fcasson/jetto/jet/92398/mar1819/seq#7	3425	4.5 MW IC	High
92398 rotation, SCENIC IC res scan	15 cm HFS	fcasson/jetto/jet/92398/mar1819/seq#9	3427	4.5 MW IC	High
85307 rotation, SCENIC IC res scan	30 cm LFS	fcasson/jetto/jet/92398/jun0719/seq#1	3450	4.5 MW IC	Low
85307 rotation, SCENIC IC res scan	10 cm LFS	fcasson/jetto/jet/92398/jun0719/seq#2	3451	4.5 MW IC	Low
85307 rotation, SCENIC IC res scan	Axial	fcasson/jetto/jet/92398/jun0719/seq#3	3452	4.5 MW IC	Low
85307 rotation, SCENIC IC res scan	15 cm HFS	fcasson/jetto/jet/92398/jun0719/seq#4	3453	4.5 MW IC	Low

Tests of the impact on W asymmetry of different anisotropy models (as shown in appendix 3):

Description	IC resonance	JETTO ID	PPF seq. no.	Heating	Rotation
Dendy model + SCENIC anisotropy	30 cm LFS	fcasson/jetto/jet/92398/mar1819/seq#15	3640	4.5 MW IC	None
Dendy model + SCENIC anisotropy	10 cm LFS	fcasson/jetto/jet/92398/mar1819/seq#16	3641	4.5 MW IC	None
Dendy model + SCENIC anisotropy	Axial	fcasson/jetto/jet/92398/mar1819/seq#17	3642	4.5 MW IC	None
Dendy model + SCENIC anisotropy,	15 cm HFS	fcasson/jetto/jet/92398/mar1819/seq#18	3643	4.5 MW IC	None
Geom. adapted model + SCENIC anisotropy	30 cm LFS	fcasson/jetto/jet/92398/mar1819/seq#10	3428	4.5 MW IC	None
Geom. adapted model + SCENIC anisotropy	10 cm LFS	fcasson/jetto/jet/92398/mar1819/seq#11	3429	4.5 MW IC	None
Geom. adapted model + SCENIC anisotropy	Axial	fcasson/jetto/jet/92398/mar1819/seq#12	3430	4.5 MW IC	None
Geom. adapted model + SCENIC anisotropy	15 cm HFS	fcasson/jetto/jet/92398/mar1819/seq#13	3431	4.5 MW IC	None

ORCID iDs

F.J. Casson  <https://orcid.org/0000-0001-5371-5876>
H. Patten  <https://orcid.org/0000-0001-5600-2097>
A. Czarnecka  <https://orcid.org/0000-0003-4931-728X>
O. Ficker  <https://orcid.org/0000-0001-6418-9517>
L. Frassinetti  <https://orcid.org/0000-0002-9546-4494>
L. Garzotti  <https://orcid.org/0000-0002-3796-9814>
J.P. Graves  <https://orcid.org/0000-0002-7959-7959>
T. Johnson  <https://orcid.org/0000-0002-7142-7103>

References

- [1] Joffrin E. et al 2019 *Nucl. Fusion* **59** 112021
[2] Angioni C. et al 2014 *Nucl. Fusion* **54** 083028
[3] Angioni C. et al 2015 *Phys. Plasmas* **22** 055902
[4] Romanelli M. and Ottaviani M. 1998 *Plasma Phys. Control. Fusion* **40** 1767
[5] Breton S. et al 2018 *Nucl. Fusion* **58** 096003
[6] Casson F.J. et al 2015 *Plasma Phys. Control. Fusion* **57** 014031
[7] Angioni C. and Helander P. 2014 *Plasma Phys. Control. Fusion* **56** 124001
[8] Bilato R. et al 2017 *Nucl. Fusion* **57** 056020
[9] Belli E.A. and Candy J. 2008 *Plasma Phys. Control. Fusion* **50** 095010
[10] Belli E.A. and Candy J. 2009 *Plasma Phys. Control. Fusion* **51** 075018
[11] Belli E.A. and Candy J. 2012 *Plasma Phys. Control. Fusion* **54** 015015
[12] Bourdelle C. et al 2016 *Plasma Phys. Control. Fusion* **58** 014036
[13] Citrin J. et al 2017 *Plasma Phys. Control. Fusion* **59** 124005
[14] Cenacchi G. and Taroni A. 1988 *JET Intern. Rep. JET-IR* **88** 3
[15] Romanelli M. et al 2014 *Plasma Fusion Res.* **9** 3403023
[16] Citrin J. et al 2014 *Plasma Phys. Control. Fusion* **57** 014032
[17] Citrin J. et al 2013 *Phys. Rev. Lett.* **111** 155001
[18] Wilkie G.J., Iantchenko A., Abel I.G., Highcock E. and P. I. 2018 *Nucl. Fusion* **58** 082024
[19] Whelan G.G., Pueschel M.J. and Terry P.W. 2018 *Phys. Rev. Lett.* **120** 175002
[20] Siena A.D. et al 2019 *Nucl. Fusion* **59** 124001
[21] Challis C.D. et al 1989 *Nucl. Fusion* **29** 563
[22] Eriksson L.-G., Hellsten T. and Willen U. 1993 *Nucl. Fusion* **33** 1037
[23] Eriksson L.-G. and Hellsten T. 1995 *Phys. Scr.* **52** 70
[24] Tamor S. 1981 *J. Comput. Phys.* **40** 104
[25] Pütterich T. et al 2013 *Plasma Phys. Control. Fusion* **55** 124036
[26] Pütterich T. et al 2012 24th IAEA Fusion Energy Conference (San Diego, CA, 8–13 October 2012) [EX/P3.15]
[27] Erba M., Cherubini A., Parail V.V., Springmann E. and Taroni A. 1997 *Plasma Phys. Control. Fusion* **39** 261
[28] Linder O. et al 2018 *Nucl. Fusion* **59** 016003
[29] Kirov K.K. et al 2019 *Nucl. Fusion* **59** 056005
[30] Sertoli M. et al 2011 *Plasma Phys. Control. Fusion* **53** 035024
[31] Sertoli M., Dux R., Pütterich T. and The A. U. Team 2015 *Plasma Phys. Control. Fusion* **57** 075004
[32] Hender T.C. et al 2016 *Nucl. Fusion* **56** 066002
[33] Angioni C. et al 2017 *Nucl. Fusion* **57** 056015
[34] Brambilla M. and Bilato R. 2009 *Nucl. Fusion* **49** 085004
[35] Brambilla M. and Bilato R. 2006 *Nucl. Fusion* **46** S387
[36] Cooper W.A. et al 2006 *Nucl. Fusion* **46** 683
[37] Jucker M. et al 2011 *Comput. Phys. Commun.* **182** 912
[38] Mantsinen M.J. et al 1999 *Plasma Phys. Control. Fusion* **41** 843
[39] Patten H.W. 2019 Development and optimisation of advanced auxiliary ion heating schemes for 3D fusion plasma devices *Ph.D. EPFL* (<https://infoscience.epfl.ch/record/263665>)
[40] Puiatti M.E. et al 2006 *Phys. Plasmas* 1994–Present **13** 042501
[41] Lerche E. et al 2016 *Nucl. Fusion* **56** 036022
[42] Eester D.V. et al 2017 *EPJ Web Conf.* **157** 03061
[43] Goniche M. et al 2017 *Plasma Phys. Control. Fusion* **59** 055001
[44] Sertoli M. et al 2018 Effects of the ICRH resonance position on the profile shape of the W density in JET-ILW H-mode discharges *45th EPS Conference on Plasma Physics* (Prague, Czech Republic, 2–6 July 2018) O4.103 (<http://ocs.ciemat.es/EPS2018PAP/pdf/O4.103.pdf>)
[45] Breton S. et al *Phys. Plasmas* **25** 2018 012303
[46] Gallart D. et al 2018 *Nucl. Fusion* **58** 106037
[47] Angioni C. et al 2012 *Nucl. Fusion* **52** 114003
[48] Angioni C. 2015 *Phys. Plasmas* 1994–Present **22** 102501
[49] Roach C.M. et al 2009 *Plasma Phys. Control. Fusion* **51** 124020
[50] Bourdelle C. et al 2018 *Nucl. Fusion* **58** 076028
[51] Kamelander G. and Sigmar D. 1992 *J. Phys. Scr.* **45** 147
[52] Schneider P.A. et al 2017 *Nucl. Fusion* **57** 066003
[53] Angioni C., Fable E., Manas P., Mantica P. and Schneider P.A. 2018 *Phys. Plasmas* **25** 082517
[54] Belli E.A., Candy J. and Waltz R.E. 2019 *Phys. Plasmas* **26** 082305
[55] Garcia J. et al 2019 *Nucl. Fusion* **59** 086047
[56] Howard N.T., Holland C., White A.E., Greenwald M. and Candy J. 2015 *Plasma Phys. Control. Fusion* **57** 065009
[57] Howard N.T., Holland C., White A.E., Greenwald M. and Candy J. 2016 *Nucl. Fusion* **56** 014004
[58] Bonanomi N., Mantica P., Citrin J., Goerler T. and T B. 2018 *Nucl. Fusion* **58** 124003
[59] Maggi C.F. et al 2018 *Plasma Phys. Control. Fusion* **60** 014045

- [60] Weisen H. *et al* 2018 Isotope dependence of confinement in JET-ILW deuterium and hydrogen plasmas *27th IAEA Fusion Energy Conf.* (Gandhinagar, India, 22–27 October 2018) [EX/P1-4] (https://conferences.iaea.org/indico/event/151/papers/5859/files/5124-IAEA_isotope_8p_corrected.pdf)
- [61] Bustos A., Bañón Navarro A., Görler T., Jenko F. and Hidalgo C. 2015 *Phys. Plasmas* **22** 012305
- [62] Garcia J., Görler T., Jenko F. and Giruzzi G. 2017 *Nucl. Fusion* **57** 014007
- [63] Frassinetti L. *et al* 2018 The EUROfusion JET-ILW pedestal database *45th EPS Conference on Plasma Physics* (Prague, Czech Republic, 2–6 July 2018) P4.1027 (<http://ocs.ciemat.es/EPS2018PAP/pdf/P4.1027.pdf>)
- [64] Garcia J. *et al* 2017 *Plasma Phys. Control. Fusion* **59** 014023
- [65] Cordey J.G. *et al* 2003 *Nucl. Fusion* **43** 670
- [66] Casson F.J. *et al* 2018 Predictive multi-channel flux-driven modelling to optimise ICRH tungsten control in JET *Preprint: 2018 IAEA Fusion Energy Conf.* (Gandhinagar, India, 22–27 October 2018) TH/3-2 (<https://conferences.iaea.org/event/151/contributions/6118/>)
- [67] Ho A. *et al* 2019 *Nucl. Fusion* **59** 056007
- [68] Casson F.J. 2011 Turbulent transport in rotating tokamak plasmas *Ph.D.* University of Warwick (<http://wrap.warwick.ac.uk/36765/>)
- [69] Angioni C., Casson F.J., Veth C. and Peeters A.G. 2012 *Phys. Plasmas* **19** 122311
- [70] Casson F.J. *et al* 2010 *Phys. Plasmas* **17** 102305
- [71] Reinke M.L. *et al* 2012 *Plasma Phys. Control. Fusion* **54** 045004
- [72] Dendy R.O., Hastie R.J., McClements K.G. and Martin T.J. 1995 *Phys. Plasmas* **2** 1623
- [73] Graves J.P., Cooper W.A., Coda S., Eriksson L.G. and Johnson T. 2006 *AIP Conf. Proc.* **871** 350